ARTICLE IN PRESS

Nature Communications

https://doi.org/10.1038/s41467-026-68516-y

Article in Press

Engineering energy-efficient *Saccharomyces cerevisiae* for methanol and CO_2 assimilation

Received: 15 May 2025

Accepted: 8 January 2026

Cite this article as: Zhong, W., Liu, N., Chen, B. *et al.* Engineering energy-efficient *Saccharomyces cerevisiae* for methanol and CO_2 assimilation. *Nat Commun* (2026). https://doi.org/10.1038/s41467-026-68516-y

Wei Zhong, Nana Liu, Binbin Chen, Huiqi Sun, Xiao Fei, Jiazhang Lian, Junling Guo, Bo Wang & Yajie Wang

We are providing an unedited version of this manuscript to give early access to its findings. Before final publication, the manuscript will undergo further editing. Please note there may be errors present which affect the content, and all legal disclaimers apply.

If this paper is publishing under a Transparent Peer Review model then Peer Review reports will publish with the final article.

ARTICLE IN PRESS

© The Author(s) 2026. **Open Access** This article is licensed under a Creative Commons Attribution-NonCommercial-NoDerivatives 4.0 International License, which permits any non-commercial use, sharing, distribution and reproduction in any medium or format, as long as you give appropriate credit to the original author(s) and the source, provide a link to the Creative Commons licence, and indicate if you modified the licensed material. You do not have permission under this licence to share adapted material derived from this article or parts of it. The images or other third party material in this article are included in the article's Creative Commons licence, unless indicated otherwise in a credit line to the material. If material is not included in the article's Creative Commons licence and your intended use is not permitted by statutory regulation or exceeds the permitted use, you will need to obtain permission directly from the copyright holder. To view a copy of this licence, visit http://creativecommons.org/licenses/by-nc-nd/4.0/.

Engineering energy-efficient *Saccharomyces cerevisiae* for methanol and CO_2 assimilation

Wei Zhong[1,2], Nana Liu[1,2], Binbin Chen[1,2], Huiqi Sun[3], Xiao Fei[1,2], Jiazhang Lian[4,5], Junling Guo[6], Bo Wang[7], Yajie Wang[1,2,3,8*]

[1] Center of Synthetic Biology and integrated Bioengineering, Westlake University, Hangzhou, Zhejiang, 310030, China

[2]School of Engineering, Westlake University, Hangzhou, Zhejiang, 310030, China

[3]Center for Future Food, Muyuan Laboratory, Zhengzhou, Henan, 450007, China

[4]Key Laboratory of Biomass Chemical Engineering of Ministry of Education, College of Chemical and Biological Engineering, Zhejiang University, Hangzhou, Zhejiang, 310027, China

[5]State Key Laboratory of Coordination Chemistry, School of Chemistry and Chemical Engineering, Nanjing University, Nanjing, Jiangsu, 210093, China

[6]BMI Center for Biomass Materials and Nanointerfaces, National Engineering Laboratory for Clean Technology of Leather Manufacture, Ministry of Education Key Laboratory of Leather Chemistry and Engineering, College of Biomass Science and Engineering, Sichuan University, Chengdu, Sichuan, 610065, China

[7]State Key Laboratory of Quantitative Synthetic Biology, Center for Materials Synthetic Biology, Shenzhen Institute of Synthetic Biology, Shenzhen Institute of Advanced Technology, Chinese Academy of Sciences, Shenzhen, Guangzhou, 518055, China

[8]School of Life Science, Westlake University, Hangzhou, Zhejiang, 310000, China

*Corresponding author: wangyajie@westlake.edu.cn

Abstract

Methanol is a promising one-carbon (C1) feedstock for microbial bioconversion; however, engineered *Saccharomyces cerevisiae* often faces energetic constrains during its assimilation. Here, we develop SC-AOX$_{25}$, an energy-efficient methylotrophic *S. cerevisiae*, through engineering of heterologous methanol-formaldehyde-formate (MFF) oxidation pathways coupled with adaptive laboratory evolution. SC-AOX$_{25}$ efficiently generates adenosine triphosphate (ATP) and nicotinamide adenine dinucleotide (NADH) during methanol metabolism while co-assimilating methanol-derived intermediates (formaldehyde, formate, and CO_2) via native glyoxylate-serine cycle, pentose phosphate pathway, and reductive glycine pathway. Key energy modules - Fdh1$_{sc}$, Adh2$_{m}$, Aox$_{m}$, and Rgi2$_{m}$ - are characterized for their roles in ATP/NADH synthesis and methylotrophic growth. Formaldehyde-induced DNA-protein crosslinks (DPCs) and large repeated DNA fragments suggest strategies for methanol detoxification and phenotype enhancement. Utilizing SC-AOX$_{25}$, we enable CO_2 assimilation through non-native Calvin cycle during methanol fermentation, establishing the engineered strain as a robust and energy-efficient methylotrophic platform for further C1 engineering.

Introduction

Anthropogenic climate change remains a critical issue of the 21st century. The “State of Climate Action 2023” report by the World Resources Institute indicates that global efforts are falling short. Accelerating the phase-out of fossil fuels, expanding renewable energy, and transforming food systems are essential to meet the 2030 climate goals[1]. Bioconversion of non-food feedstocks offers potential for cost-effective, carbon-negative chemical production, reducing pressure on strained agricultural resources. Green methanol is particularly promising due to the wide availability of renewable feedstocks (like biomass, CO_2, and green hydrogen), its sustainable production methods, and compatibility with existing transportation and fermentation infrastructures[2-6]. Recently, significant progresses have been made in developing genetic tools for native methylotrophic organisms like *Methylobacterium extorquens*[7-9], *Bacillus methanolicus*[10,11], *Hansenula polymorpha*[12,13], and *Pichia pastoris*[12,14-16]. However, many of them are still not adequately characterized, or their intrinsic methanol conversion efficiency and capabilities to produce high-value-added chemicals remain limited. Over the past decade, there has been growing interest in engineering methylotrophy in industrial glycolytic bacteria and yeast to produce value-added products from methanol. While notable progresses have been made with prokaryotic organisms like *Escherichia coli*[17-19], success has been more limited with eukaryotic model systems[20-23].

Engineering *Saccharomyces cerevisiae* for methylotrophy presents a significant scientific challenge and substantial industrial benefits. *S. cerevisiae* is valued for its advanced protein folding and modification capabilities, a well-established gene editing framework, and exceptional adaptability to demanding fermentation conditions, including resistance to low pH and solvents[24-26]. Different strategies have been applied to convert *S. cerevisiae* into methylotrophy, such as the engineered module circuit strategy combined with adaptive laboratory evolution[20,22,23,27] and the introduction of synthetic C1-compound assimilation pathways[21,28]. However, shutting down the glycolysis pathway can cause an immediate energy imbalance[29,30], resulting in insufficient energy for ATP- or NADH-dependent enzymatic reactions in methanol assimilation pathways, as well as the biosynthesis of amino acids, vitamins, and cofactors essential for healthy cell growth[31,32]. As a result, synthetic methylotrophic *S. cerevisiae* variants exhibit a slow growth rate, long doubling time, and require additional yeast extract[20-23].

Several heterologous pathways have been explored to engineer *E. coli* for methylotrophic growth, including the reductive glycine (rGly) pathway [33], the modified serine cycle[34], the homoserine cycle[35], the serine-threonine cycle etc.[36,37]. Among these, expressing the native ribulose monophosphate pathway (RuMP) from methylotrophic bacteria, followed by adaptive evolution, has proven the most successful strategy for developing industrial viable methylotrophic *E. coli*[17-19]. These successes highlight the importance of natural, well-adapted pathways in engineering methylotrophy in industrial glycolytic microorganisms. Inspired by the recent findings that *S. cerevisiae* can assimilate methanol via the native pentose phosphate pathway (PPP)[22], we propose equipping *S. cerevisiae* with an efficient energy module while leveraging its inherent metabolic capabilities to enhance methanol assimilation efficiency, ultimately creating a superior platform for engineering methylotrophic *S. cerevisiae.*

In this study, we engineer the energy-efficient methylotrophic *S. cerevisiae*, SC-AOX$_{25}$, by integrating a heterologous methanol-formaldehyde-formate (MFF) oxidation pathway and applying adaptive laboratory evolution (ALE). SC-AOX$_{25}$ achieve the specific growth rate of 0.021 h^{-1} (equivalent to a 33.0 h doubling time) and the final OD$_{600}$ of 1.11 from 0.05 in minimal medium (MM) with methanol, surpassing previous studies[20-23]. Using SC-AOX$_{25}$, we map the complete native methanol assimilation pathways in *S. cerevisiae* , including the glyoxylate-serine cycle (GSC), the pentose phosphate pathway (PPP), and the rGly pathways, with GSC and PPP as primary routes. We demonstrate that SC-AOX$_{25}$ efficiently generates ATP and NADH to sustain its methylotrophic growth. Key energy modules – Fdh1$_{sc}$, Adh2$_{m}$, Aox$_{m}$, and Rgi2$_{m}$ (promoter and terminator mutation)– are also characterized for their roles in ATP/NADH synthesis, methanol assimilation, and cell growth. Additionally, well-characterized formaldehyde-induced DNA-protein crosslinks (DPCs) and large repeated DNA fragments suggest potential strategies for methanol detoxification and phenotype enhancement. By integrating the non-native Calvin-Benson-Bassham (CBB) cycle into SC-AOX$_{25}$, we enhance methanol assimilation efficiency via CO$_2$ co-utilization, establishing this engineered strain as an energy-efficient platform for further C1 engineering.

Results

Construction of MFF oxidation pathway and rapid-growth methylotrophic *S. cerevisiae*

Clean methanol, with an energy density of 23 MJ/kg[38] - higher than glucose's 15.5 MJ/kg[39] - plays a vital role in achieving net-zero emission targets by aiding the decarbonization of the energy and chemical sectors[40]. Inspired by this, we introduced two distinct methanol oxidation pathways into the cytoplasm of *S. cerevisiae* to generate energy for C1 compounds fixation. The first pathway is O$_2$-dependent, where methanol is oxidized to formaldehyde by alcohol oxidase (Aox) from *H. polymorpha*, activated by pyruvate carboxylase (Pyc1) from the same organism[41]. Catalase (Cat) from *H. polymorpha* was overexpressed to neutralize the toxicity of H$_2$O$_2$. The second pathway is NAD$^+$-dependent, utilizing methanol dehydrogenase (Mdh3) from *B. methanolicus*, activated by its activator protein Act1[42]. In both pathways, formaldehyde is further oxidized to CO$_2$ by formaldehyde dehydrogenase (Fld1) and *S*-formylglutathione hydrolase (Fgh1) from *P. pastoris*, and formate dehydrogenase (Fdh1) from *H. polymorpha* (Fig. 1a). The mRNA levels in SC-AOX$_0$ and SC-MDH$_0$ were evaluated to ensure the proper transcription of these heterologous genes under physiological conditions (Supplementary Fig. 1). The enzymatic activities for Aox, Mdh3, Fld1, Fdh1, Cat, and Fgh1 were measured at 67 (±5), 52 (±3), 33 (±3), 63 (±4), 29 (±3), and 160 (±3) mU/mg, respectively (Fig. 1b), confirming the functionality of these key enzymes.

The SC-AOX$_0$ and SC-MDH$_0$ did not grow in MM with 5~10 g/L methanol, likely due to methanol toxicity and slow assimilation rates (Supplementary Fig. 2). To obtain methylotrophic mutants, we performed adaptive laboratory evolution (ALE) on SC-AOX$_0$, SC-MDH$_0$, and CEN.PK2-1C. ALE occurred in two stages: Stage I selected variants capable of utilizing 10 g/L methanol, while Stage II identified strains with high tolerance and rapid growth in 20 g/L methanol (Supplementary Fig. 3). After 8 rounds and 64 days of evolution in Stage I, SC-AOX$_I$ exhibited slow growth with a doubling time of about 52.2 hours (Fig. 1c). SC-AOX$_I$ was further evolved 14 generations (approximately 60 days) in Stage II, resulting in SC-AOX$_{II}$, which showed significantly shorter doubling times of about 38.1 hours (Fig. 1c). In contrast, SC-MDH$_0$ and CEN.PK2-1C evolved more slowly, with no significant growth observed after 120 days.

We isolated single colonies SC-AOX$_9$ and SC-AOX$_{25}$, which showed superior growth in the MM with 10 g/L methanol, from SC-AOX$_I$ and SC-AOX$_{II}$, respectively (Supplementary Fig. 4). Fermentation profiles indicated that SC-AOX$_9$ and SC-AOX$_{25}$ reached OD$_{600}$ values of 0.65 (± 0.014) and 1.11 (± 0.03) from an initial OD$_{600}$ of 0.08 within five days (Supplementary Table 1). SC-AOX$_{25}$ achieved a maximum specific growth rate of 0.0210 ± 0.0003 h^{-1} (equivalent to a doubling time of 33.0 ± 0.3 h), consuming 4.02 ± 0.38 g/L of methanol over five days (Fig. 1d; Supplementary Fig. 5). Among engineered methylotrophic *S. cerevisiae*, SC-AOX$_{25}$ achieves a higher OD$_{600}$ and shorter doubling time than strains reported in previous studies (Supplementary Table 1)[20,21,23].

Elucidation of the methanol assimilation pathways in the SC-AOX$_{25}$

It has been reported that *S. cerevisiae* has endogenous pathways for methanol assimilation, such as converting methanol to formaldehyde, which then enters the pentose phosphate[22]. However, a comprehensive global metabolic network of endogenous methanol metabolism in *S. cerevisiae* is not fully characterized, including both known and potentially undiscovered routes with their quantitative contributions. To elucidate the metabolic pathways involved in methanol assimilation in SC-AOX$_{25}$, we performed various ^{13}C labeling experiments using 10 g/L ^{13}C-MeOH in MM. Isotopic labeling analysis revealed ^{13}C incorporation into nine amino acids, with L-threonine and L-serine exceeding 20% labeling fractions (Fig. 2a and Supplementary Fig. 6). Additionally, fourteen central metabolites were labeled, including key TCA cycle metabolites like succinic acid, fumaric acid, citric acid, isocitric acid, and aconitic acid, all exhibiting more than 10% ^{13}C-incorportaion (Fig. 2b and Supplementary Fig. 6). These labeling patterns demonstrate active methanol-derived carbon flux through both amino acid biosynthesis and core energy metabolism pathways. Furthermore, transcriptomic profiling of SC-AOX$_{25}$ cultured on methanol revealed significant upregulation of key TCA cycle genes, including *IDP2*, *IDP3*, *PCK1*, *CIT3*, *KGD1*, and *LSC2*, compared to those cultured in MM with glucose (Supplementary Fig. 7). This indicates reinforcement of central carbon metabolism under methylotrophic conditions.

Based on the ^{13}C labeling and transcriptomic analysis, we hypothesized that methanol could be assimilated through the three pathways: the PPP, the GSC, and the rGly (Fig. 3). Formaldehyde, oxidized from partial MFF, can be assimilated through the PPP and enter the TCA cycle (Fig. 3). ^{13}C-MeOH labeling experiments showed that some key metabolites in the PPP, such as fructose-6-phosphate, fructose 1,6-bisphosphate, and ribose 5-phosphate were labeled at 6.3%, 4.2%, and 7.5%, respectively (Fig. 2b). Transcriptomic data revealed a 4.6-fold upregulation of *TKL2* and a 4.8-fold upregulation of *ALD4* (Supplementary Fig. 7 and Fig. 3). Given that Tkl2 is a transketolase (which catalyzes conversion of xylulose-5-phosphate (Xu5P) and ribose-5-phosphate to sedoheptulose-7-phosphate and glyceraldehyde-3-phosphate in PPP[45]) and Ald4 is an aldehyde dehydrogenase (which catalyzes acetaldehyde to acetate[46]), we hypothesized that these enzymes might also catalyze novel chemical transformations involving formaldehyde and Xu5P. To evaluate this hypothesis, we conducted *in vitro* enzymatic assays using recombinantly expressed Tkl1, Tkl2, and Ald4. These experiments confirmed that both Tkl1 and Tkl2 catalyze the conversion of formaldehyde and Xu5P to DHA and GAP, whereas Ald4 showed no such activity (Supplementary Fig. 8). Although deletion of *TKL1*/*TKL2* led to severe growth impairment on methanol relative to the SC-AOX$_{25}$ strain (Supplementary Fig. 9a), the growth defect per se could not be unequivocally linked to disruption of the PPP (Supplementary Fig. 10). Collectively, the demonstrated capability of Tkl1/Tkl2 to assimilate formaldehyde with Xu5P into DHA and

GAP provides direct evidence supporting methanol assimilation via the PPP (Supplementary Fig. 8).

Formate derived from the MFF undergoes dual metabolic fates in SC-AOX$_{25}$: cytoplasmic assimilation via the trifunctional Ade3, converting formate to serine for entry into the GSC, and mitochondrial import where it is incorporated into glycine through the rGly pathway coupled with CO_2 fixation. To validate GSC-mediated methanol assimilation, ^{13}C-labeling experiments were performed in MM with ^{13}C-formate/^{12}C-MeOH without serine and glycine. The results indicated that ^{13}C-incorportion into twelve amino acids and eleven central metabolic intermediates (Fig. 2c-d and Supplementary Fig. 6). Serine exhibited the highest labeling efficiency (30%), and transcriptomic analysis revealed a 17.3-fold upregulation of *CHA1* in the rGly pathway (Supplementary Fig. 7), suggesting that the rGly pathway may exist and further contribute to serine synthesis. To confirm this, $^{13}CO_2$-labeling experiments were conducted using MM with $NaH^{13}CO_3$/^{12}C-MeOH (serine and glycine omitted). Results showed label incorporation into glycine (0.68%), serine (8%), and TCA cycle metabolites (Fig. 2e-f and Supplementary Fig. 6). While *S. cerevisiae* can assimilate CO_2/HCO_3^- via pyruvate carboxylase, yielding oxaloacetate for energy metabolism[47], or acetyl-CoA carboxylase for lipid biosynthesis[48], the labeled products, palmitic acid (1%) from lipid synthesis and oxaloacetate (0%) from carboxylase-mediated CO_2 fixation, were detected at very low levels (Supplementary Fig. 6f). Thus, the observed glycine (0.68%) /serine (8%) labeling is most likely due to the rGly pathway activity, as these routes are distinct from protein synthesis. This conclusively demonstrates rGly's role in amino acid synthesis during methylotrophy.

Transcriptomic analysis was conducted to assess the relative contributions of the GSC and rGly in formate assimilation. Compared to SC-AOX$_{25}$ in glucose, those cultured in methanol showed more than tenfold upregulation of key GSC genes, including malate synthase (*MLS1*), isocitrate lyase (*ICL1*), serine/threonine dehydratase (*CHA1*), and alanine:glyoxylate aminotransferase (*AGX1*)

(Fig. 3 and Supplementary Fig. 7). In contrast, genes associated with the rGly pathway showed no significant changes, except *CHA1* (Fig. 3 and Supplementary Fig. 7). Additionally, deletion of *ADE3*, encoding enzyme for converting formate to 5,10-Methylene-THF in the GSC, significantly reduced growth. In contrast, knocking out the key gene *MIS1* in the rGly pathway showed no changes in growth phenotype (Supplementary Fig. 9a). These results collectively demonstrate that formate assimilation in SC-AOX$_{25}$ occurs predominantly through the GSC rather than the rGly pathway in *S. cerevisiae*.

Characterization of the energy module and its correlation with methanol assimilation in SC-AOX$_{25}$

We hypothesized that a sufficient energy supply supports the methylotrophic growth of AOX$_{25}$. To validate this and characterize the key energy modules, we conducted ^{13}C labeling experiments, confirming that both ATP and NADH can be synthesized from methanol (Fig. 2b and Fig. 2d). Further characterization during exponential growth phase revealed that SC-AOX$_{25}$ produced about 4.6 and 5.4 times more ATP in MM with methanol compared to glucose or methanol plus glucose, respectively (Fig. 4a). It also showed significantly higher ATP levels-9.0-fold for SC-AOX$_0$ and 7.4-fold for CEN.PK2-1C under MM with methanol plus glucose (Fig. 4a), indicating pronounced methanol-induced upregulation of ATP synthesis in SC-AOX$_{25}$ and suggesting enhanced metabolic efficiency under methanol fermentation. In addition, SC-AOX$_{25}$ exhibited lower NADH concentrations in methanol-based MM compared to glucose or combined glucose and methanol media, likely due to the stronger NADH production capacity of glycolytic carbon metabolism compared to methanol oxidation. Under aerobic respiration, 1 mol of glucose is fully oxidized to produce 8 mol of NADH, whereas MFF yields only 2 mol of NADH per mole consumed[42,49]. Interestingly, SC-AOX$_{25}$ displayed significantly elevated NADH and ATP levels in MM with glucose compared to SC-AOX$_0$ and CEN.PK2-1C (Fig. 4a-b). These results suggest that the SC-AOX$_{25}$ possesses improved NADH and ATP yield in glycolytic metabolism too.

We next explored the key modules contributing to ATP/NADH enhancement and methanol utilization. Formate oxidation plays a key role in formate detoxification and NADH production. Deletion of heterologous $FDH1_{hp}$ resulted in growth arrest in SC-AOX$_{25}$-Δ$FDH1_{hp}$, whereas disruption of the endogenous FDH1$_{sc}$ in strain SC-AOX$_{25}$ only attenuated growth without inducing stasis (Supplementary Fig. 9b), indicating the importance of heterologous MFF in methanol assimilation. Additionally, the transcriptomic analysis showed that endogenous $FDH1_{sc}$ was upregulated about 565.2-fold in SC-AOX$_{25}$ grown on methanol (Supplementary Fig. 7). Knocking out $FDH1_{sc}$ reduced the methanol consumption and the final OD$_{600}$ of SC-AOX$_{25}$-Δ$FDH1_{sc}$ by 6.4-fold and 7.8-fold, respectively (Fig. 4c-d). This may be attributed to formate toxicity, as a 1.7-fold accumulation of formate occurred in SC-AOX$_{25}$-Δ$FDH1_{sc}$ compared to SC-AOX$_{25}$ during methanol fermentation (Supplementary Fig. 11). Additionally, NADH and ATP concentrations in SC-AOX$_{25}$-Δ$FDH1_{sc}$ were reduced by 1.5-fold and 6.7- fold, respectively, in MM with methanol, and by 2.0-fold and 4.8- fold, respectively in MM with glucose plus methanol (Fig. 4e-f). These findings demonstrate the crucial role of Fdh1$_{sc}$ in ATP/NADH generation, methanol consumption, and methylotrophic growth.

Whole-genome sequencing (WGS) revealed mutations in 3.0% of bases in endogenous *ADH2* and 1.6% of bases in heterologous expressed *AOX* compared to reference sequences. Transcriptomic analysis showed that $ADH2_m$ and AOX_m were upregulated by approximately 192.7- and 2.8-fold, respectively, in SC-AOX$_{25}$ grown on methanol (Supplementary Data 1). Since both are involved in alcohol oxidation and NADH production, we speculated that Adh2$_m$ and Aox$_m$ may assist in energy metabolism and methanol assimilation in SC-AOX$_{25}$. The knockout mutants SC-AOX$_{25}$-Δ$ADH2_m$ and SC-AOX$_{25}$-ΔAOX_m grew more slowly, with doubling times doubled and final OD$_{600}$ reduced to 0.83 and 0.78, respectively (Fig. 4c and Supplementary Fig. 9c). Additionally, their methanol consumption decreased by 3.7-fold and 5.6-fold, respectively (Fig. 4d). While the NADH concentration in the exponential phase of SC-AOX$_{25}$-Δ$ADH2_m$ and SC-AOX$_{25}$-ΔAOX_m was similar to that of SC-AOX$_{25}$, their ATP levels were reduced by 25-fold and 14-fold, respectively (Fig. 4e-f). These findings indicate that $Adh2_m$ and Aox_m are closely related to energy metabolism and methanol assimilation.

To further validate the functions of those mutants, we overexpressed *ADH2ₘ* and *AOXₘ* in SC-AOX_0. Although SC-AOX_0-$ADH2_m$ and SC-AOX_0-AOX_m did not grow in MM with 10 g/L methanol, SC-AOX_0-$ADH2_m$-AOX_m showed significant growth, reaching a final OD_{600} of 0.49 within 120 hours without evolution (Fig. 4c and Supplementary Fig. 9c). Since SC-AOX_0 did not grow in MM with methanol, we compared the ATP and NADH levels between SC-AOX_0-$ADH2_m$-AOX_m and SC-AOX_0 in MM with 10 g/L methanol plus 20 g/L glucose. Notably, ATP and NADH levels in SC-AOX_0-$ADH2_m$-AOX_m were elevated by 2.1-fold and 1.8-fold, respectively (Fig. 4e-f). To elucidate the mechanism behind these improvements, we conducted kinetic studies on purified $Adh2_m$ and Aox_m. The specific activity and catalytic efficiency of Aox_m on methanol were about two and four times higher than the wild type, respectively (Supplementary Fig. 12a-b). Additionally, $Adh2_m$ exhibits 2.2-fold higher specific activity towards methanol, producing three times more formaldehyde (Supplementary Fig. 12c). These results suggest that the $Adh2_m$ and Aox_m enhance the methanol oxidation efficiency, thereby contributing to energy production and methylotrophic growth. Although no significant structural alterations were observed (Supplementary Fig. 12d), we hypothesize that the enhanced catalytic activity of $Adh2_m$ toward methanol may result from subtle modifications in the active-site pocket, leading to improved binding and catalytic proficiency for methanol (Supplementary Fig. 12e).

Aside from genes related to methanol and formate oxidation, we presume that the evolved SC-AOX_{25} may have additional regulatory mechanisms to enhance energy production and methanol assimilation. WGS and transcriptomic analysis revealed an uncharacterized mutant, $RGI2_m$ (promoter and terminator mutation), with transcriptional levels upregulated by 1276-fold (Supplementary Data 1). Rgi2 has been previously proposed to respond to stress conditions and might be involved in yeast energy metabolism[50,51]. To determine whether $Rgi2_m$ is related to energy metabolism and methanol assimilation in SC-AOX$_{25}$, we constructed Rgi2$_{m}$ knock-in and knock-out mutants and measured the ATP/NADH levels, methanol consumptions, and methylotrophic growth phenotypes. Results showed that the maximum OD$_{600}$ and methanol consumption in the *RGI2$_{m}$* knockout mutant SC-AOX$_{25}$-*ΔRGI2$_{m}$* was about 0.47 and 0.32 times lower than that of SC-AOX$_{25}$ (Fig. 4c-d and Supplementary Fig. 9d), respectively. Energy assays revealed that both ATP and NADH concentrations in SC-AOX$_{25}$-*ΔRGI2$_{m}$* are much lower than in SC-AOX$_{25}$ (Fig. 4e-f), indicating that *RGI2$_{m}$* is essential for improving energy metabolism and methylotrophic growth. Additionally, overexpressing *RGI2$_{m}$* (Supplementary Fig. 13) in SC-AOX$_{0}$ results in mutant that can grow in MM with methanol to a final OD$_{600}$ of 0.32 without any evolution (Fig. 4c and Supplementary Fig. 9d). Notably, although ATP and NADH levels in SC-AOX$_{0}$-*RGI2$_{m}$* on MM with methanol are significantly higher than in SC-AOX$_{0}$ on MM with glucose plus methanol, their concentrations were lower when SC-AOX$_{0}$-*RGI2$_{m}$* was grown in MM with either methanol plus glucose or glucose alone (Fig. 4e-f). In addition, SC-AOX$_{0}$-*RGI2$_{m}$* showed negligible methanol consumption during growth in MM with methanol and glucose, suggesting carbon catabolite repression (Fig. 4d). These results demonstrate that upon glycolysis disruption in *SC-AOX$_{0}$-RGI2$_{m}$*, Rgi2$_{m}$ activates energy metabolism in response to methanol availability, sustaining methylotrophic growth through its native methanol assimilation pathways.

Given that *RGI1* is a paralog of *RGI2*, which activates energy metabolism in response to methanol, we sought to determine whether *RGI1* shares this function. We therefore constructed an *RGI1* knockout strain and assessed the resulting cellular energy status by measuring NADH and ATP levels. Disruption of *RGI1*, a paralog of *RGI2*, led to near-complete growth arrest in MM with methanol, compared to SC-AOX$_{25}$ (Supplementary Fig. 9d). In MM with glucose plus methanol, the strain showed ATP and NADH levels at 0.29-fold and 0.62-fold of SC-AOX$_{25}$, respectively (Fig. 4e–f), with minimal methanol consumption (Fig. 4d). These results suggest that Rgi1 functions similarly to Rgi2 in supporting energy metabolism during methanol assimilation, although overexpression of *RGI1* (P_{RGI1}-*RGI1*-T_{RGI1}) failed to restore growth of the SC-AOX$_0$ strain in MM with methanol (Supplementary Fig. 9d).

CBB cycle driven by the engineered methylotrophic *S. cerevisiae*

The Calvin-Benson-Bassham (CBB) is the most energy-intensive CO_2 fixation pathway, requiring 9 molar ATP and 4 molar NAD(P)H molecules per CO_2 molecule fixed[31]. To demonstrate SC-AOX$_{25}$'s potential as a synthetic methylotrophic platform for C1 assimilation, we engineered a heterologous CBB cycle for CO_2 fixation during growth on methanol. We implemented this by co-expressing heterologous ribulose-1,5-bisphosphate carboxylase/oxygenase (*RuBisCO*) from *Rhodospirillum rubrum*, phosphoribulokinase (*PRK*) from *Spinacia oleracea,* and *GroEL* and *GroES* chaperonins from *E. coli* [52,53] (Fig. 5a). Transcript analysis confirmed robust overexpression of both Rubisco and Prk (Supplementary Fig. 14), with corresponding enzymatic activities reaching 10.46 ± 0.68 U/mg (Rubisco) and 1.53 ± 0.11 U/mg (Prk) in methanol-grown cultures (Fig. 5b).

^{13}C-labeling experiments were performed to validate the functional operation of the engineered CBB cycle in SC-AOX$_{25}$-CBB. When cultured with NaH^{13}CO$_3$/^{12}C-MeOH, SC-AOX$_{25}$-CBB showed significant ^{13}C-incorporation into seven amino acids (Thr, Pro, Asn, Ser, Gly, Ala, Tyr, and Phe) and key central metabolites (F-1,6-BP, 3-PG, F6P, Acetyl-CoA, RuBP) (Fig. 5d; Supplementary Fig. 15). Specifically, the detection of labeled Ribulose-1,5-bisphosphate (RuBP), a unique intermediate exclusively synthesized by the heterologous phosphoribulokinase in the CBB cycle, provided definitive evidence of functional CO_2 fixation (Fig. 5d). Additionally, methanol fermentation results showed that the final OD$_{600}$ of the SC-AOX$_{25}$-CBB was 1.2 times of SC-AOX$_{25}$ (Fig. 5c and Supplementary Table 1) and methanol consumption also increased to 4.81 ± 0.21 g/L (Supplementary Table 1). These findings suggested that the CBB cycle potentially enhances the methanol assimilation in SC-AOX$_{25}$. Further mechanistic studies using ^{13}C-MeOH or ^{13}C-formate consistently detected ^{13}C-RuBP (Fig. 5e-f; Supplementary Fig. 15 and 16), establishing that CO_2 derived from MFF oxidative pathway could be reassimilated through the CBB cycle. These results collectively demonstrate that introducing the CBB cycle creates an additional carbon fixation node that improves methanol assimilation efficiency in SC-AOX_{25}.

The DNA-protein crosslinking problem

Methanol and its oxidation products exhibit cellular toxicity by disrupting metabolic processes, inducing DNA-protein crosslinking (DPC), promoting oxidative stress, and ultimately triggering cell death[54]. To assess the methanol toxicity in SC-AOX_{25}, we performed Scanning Electron Microscopy (SEM) on various CEN.PK2-1C mutants. While the parental strain (CEN.PK2-1C) and SC-AOX_0 showed severe membrane damage in minimal medium (MM) containing 10 g/L methanol, SC-AOX_9 and SC-AOX_{25} maintained intact cellular membranes (Supplementary Fig. 2). Furthermore, after four days of growth in MM with 10% methanol, SC-AOX_{25} exhibited superior cell viability (96.97%) compared to SC-AOX_0 (31.55%) and SC-AOX_9 (89.86%) (Supplementary Fig. 17), demonstrating its enhanced methanol tolerance.

Formaldehyde concentrations reached 821 μM/OD_{600} and 887 μM/OD_{600} in SC-AOX_9 and SC-AOX_{25} after three-day fermentation (Supplementary Fig. 18), indicating persistent formaldehyde toxicity in the evolved mutants. Given formaldehyde's reactivity with biomolecules, we hypothesized that DNA-protein crosslinks (DPCs) represent the primary mechanism of toxicity, disrupting DNA replication, transcription, translation, and ultimately leading to cell death[55]. To test this, we performed transmission electron microscopy (TEM) on genomic DNA isolated from SC-AOX_{25} at different OD_{600} during the methylotrophic fermentation in MM with 10% methanol (Fig. 6a). TEM revealed only free protein during early exponential growth. However, substantial DPC formation emerged at an OD_{600} of 0.75 and intensified at higher OD_{600} levels. When OD_{600} exceeded 1.0, formaldehyde-induced crosslinking became extremely severe, forming a web-like structure through DNA-protein-DNA or even DNA-DNA crosslinking. Notably, DPCs were more severe when mutants grew in MM with 20% methanol (Fig. 6a). In all cases, DNA strands disappeared after heating and de-crosslinking, ruling out nonspecific DNA-protein binding or image overlapping.

To systematically evaluate the impact of DPCs on SC-AOX$_{25}$'s methylotrophic growth, we isolated DPCs from biological replicates for analysis (Supplementary Fig. 17). Proteomics analysis revealed over 500 crosslinked proteins, with 17.5% shared across all four independent samples (Fig. 6b-c and Supplementary Fig. 17). Gene ontology analysis of the top 29 abundant shared proteins indicated involvement in cell wall and cytoskeleton formation, transcription and translation regulation, cell cycle progression, carbon and fatty acid metabolism, protein folding, and antioxidant and stress response pathways, all essential for proper cell proliferation[56,57]. Similar to DPCs in methylotrophic *E. coli,* which is associated with the XuMP pathway[17], the most abundant shared proteins included key PPP and GSC enzymes, such as Fdh1, Adh2, Fba1, Tdh3, Gpm1, Pgk1, Pdc1, Eno2, and Ald4 (Fig. 6b-c), with Eno2 and Pgk1 directly contributing to ATP synthesis. The abundance of these enzymes increased up to 790-fold during late log phase and at elevated methanol concentrations, suggesting that formaldehyde-induced DPCs disrupts methanol assimilation and cause a growth arrest.

Discussion

Synthetic methylotrophy in model organisms offers a sustainable route to convert greenhouse gases into valuable chemicals without competing with food resources. While *S. cerevisiae* possesses uncharacterized methanol assimilation pathways, previous engineering efforts focused on introducing heterologous pathways followed by ALE[20-23,27,28]. However, most methanol assimilation pathways require additional energy input – the PPP pathway consumes 1 molar ATP and 2 molar NADPH[58], the rGly pathway consumes 2 molar ATP and 4 molar NADH[32], and the serine cycle consumes 1 molar ATP and 1 molar NADPH[32]. Critically, disruption of glycolysis creates an immediate energy deficit, compromising methylotrophic conversion efficiency. We therefore hypothesized that instead of introducing heterologous methanol assimilation pathways, equipping *S. cerevisiae* with an efficient energy module while leveraging the *S. cerevisiae*'s inherent metabolic capabilities could be an effective strategy to enhance methanol assimilation efficiency. Thus, we introduced MFF pathway to provide NADH and ATP, enabling *S. cerevisiae* to achieve methylotrophic growth using its native methanol assimilation pathways after a short period of ALE (Supplementary Table 1). Compared to previously reported mutants[20-23,27,28], SC-AOX_{25} shows a higher specific growth rate (0.021 h^{-1}), a shorter doubling time (33.0 hours), and achieves a higher final OD_{600} (1.11) (Supplementary Table 1).

To further validate our hypothesis, we first characterized the native methanol assimilation machinery in *S. cerevisiae*. SC-AOX_{25} serves as an ideal platform for this purpose since the only heterologous pathway in SC-AOX_{25} is MFF, which produces formaldehyde, formate, and CO_2. Based on SC-AOX_{25}, we identified all methanol assimilation pathways: the PPP, the GSC, and the rGly, with PPP and GSC playing key roles in fixing formaldehyde and formate, respectively (Fig. 2 and Fig. 3). Additionally, we characterized two distinct modules critical for ATP and NADH production and methylotrophic growth. The first comprises previously uncharacterized mutants $Adh2_m$ and Aox_m, along with native $Fdh1_{sc}$, which directly elevated intracellular ATP/NADH levels through methanol oxidation, facilitating methanol-driven anabolism and cellular proliferation. Additionally, we discovered a variant, Rgi*2_m*, that activates compensatory energy metabolism in response to methanol-induced stress, enhancing biomass synthesis under substate-limiting conditions. These findings demonstrate that SC-AOX_{25} coordinates energy homeostasis with its native methanol assimilation network, achieving carbon flux repartitioning toward methanol assimilation via endogenous energy channeling. This mechanistic elucidation establishes a framework for optimizing C1 substrate-directed bio-manufacturing platforms. Analyzing the catalytic mechanism of $Rgi2_m$ is interesting for gaining deeper insights into its energy modulation mechanism and potential applications.

SC-AOX$_{25}$ presents an energy-efficient platform for methylotrophic engineering, where the MFF pathway generates formate, formaldehyde, and CO_2 that can be further assimilated through native or engineered C1 pathways to enhance carbon yield. In this study, we enhanced C1 utilization by integrating an exogenous CBB cycle, achieving successful CO_2 assimilation through CBB during methanol fermentation (Fig. 5c) and a 1.2-fold increase in final OD$_{600}$ compared to SC-AOX$_{25}$ (Fig. 5c). These results demonstrate that optimizing carbon utilization in SC-AOX$_{25}$ effectively enhances methylotrophic growth, validating its suitability as a platform for integrating heterologous C1 assimilation pathways. Despite SC-AOX$_{25}$'s robust methanol tolerance (up to 40 g/L; Supplementary Fig. 19), fermentation analysis revealed intracellular accumulation of formate and formaldehyde (Supplementary Fig. 11 and Supplementary Fig. 19), which induced toxicity via DPC formation and cellular oxidative stress. To further improve methanol utilization, future work should focus on identifying and strengthening rate-limiting steps in the PPP and GSC pathways, such as enzymes responsible for the conversion of formaldehyde to dihydroxyacetone phosphate (DHAP) and malate to glyoxylate, respectively. Additionally, overexpressing natural or artificial formate and formaldehyde assimilation pathways[59-61] could further reduce their accumulation and enhance methanol assimilation. Despite most reported pathways requiring at least 1 mol ATP, the energy-efficient SC-AOX$_{25}$ is a potential methylotrophic platform for their implementation.

In *E. coli*, formaldehyde-induced 70 kb copy number variations (CNVs) are linked to the RuMP pathway[17]. In evolved SC-AOX$_{25}$, large CNVs-beyond formaldehyde-assimilating enzymes-were associated with ATP and protein synthesis. The fragment sizes were 2 kb (3 copies), 6 kb (4 copies), 16 kb (4 copies), 18 kb (5 copies), 38 kb (5 copies), and 84 kb (5 copies) (Supplementary Table 2). The associated proteins are as follows: the *ITS* (Internal Transcribed Spacer) and *ETS* (External Transcribed Spacer) regions, which contain 35S and 25S ribosomal RNA, *TAR1* (Transcript Antisense to Ribosomal RNA), and other elements, are directly related to protein synthesis (Supplementary Fig. 20)[62,63]. The repeated 84kb mitochondrial genome sequences contain *COX1* (cytochrome c oxidase subunit), *ATP6* (F1F0 ATP synthase subunit), *OLI1* (F0 ATP synthase subunit c), and *COB* (cytochrome b) (Supplementary Fig. 20), all directly involved in mitochondrial ATP synthesis[64,65]. The functions of these repeated large fragments highlight the coordinated interplay of gene dosage intensification, metabolic network optimization, and stress tolerance enhancement in SC-AOX$_{25}$ under methanol-induced pressure. Leveraging these insights, constructing artificial chromosomes with large-scale repeats and DNA crosslinking mechanisms linked to methanol assimilation and detoxification pathways could enhance methanol tolerance and utilization efficiency in SC-AOX$_{25}$, augmenting its capacity for methanol fixation.

In conclusion, we engineered a methylotrophic *S. cerevisiae*, SC-AOX$_{25}$, capable of efficiently producing ATP and NADH during methanol fermentation. It can co-assimilate methanol, formaldehyde, formate, and CO_2 through the native GSC, PPP, and rGly pathways, achieving superior growth rate, doubling time, and final OD$_{600}$ for methylotrophic fermentation to date. The key energy modules – Fdh1$_{sc}$, Rgi2$_{m}$, Adh2$_{m}$, and Aox$_{m}$ – were characterized, contributing to ATP/NADH synthesis, methanol assimilation, and cell growth. The well-characterized formaldehyde-induced DPCs and large repeated DNA fragments also reveal potential strategies for methanol detoxification and phenotype improvement. Based on SC-AOX$_{25}$, we achieved co-assimilation of CO_2 with methanol through non-native CBB cycle, demonstrating the engineered strain as a robust, energy-efficient platform for further C1 engineering.

Methods

Plasmids, strains, and genes

S. cerevisiae CEN.PK2-1C was employed as the host strain for strain construction, while *E. coli* Trans1-T1 was utilized for plasmid construction. Complete details of all strains and plasmids used in this study are provided in Supplementary Data 2. For enzymes involved in methanol oxidation, the alcohol oxidase (Aox) and its activator pyruvate carboxylase (Pyc1) are from *H. polymorpha*. The methanol dehydrogenase (Mdh3) and its activator (Act1) are from *B. methanolicus* MGA3. For enzymes involved in the formaldehyde oxidation, formaldehyde dehydrogenase (Fld1) and *S*-

formyl glutathione hydrolase (Fgh1), which convert formaldehyde to formate, are from *P. pastoris* GS115. The formate dehydrogenase (Fdh1), which converts formate to CO_2, is from *H. polymorpha*; and the catalase (Cat), which converts hydrogen peroxide to oxygen, is from *H. polymorpha*. The non-native CBB cycle module included ribulose-1,5-bisphosphate carboxylase/oxygenase (Rubisco), which converts the condensation reaction of Ribulose-1,5-bisphosphate and CO_2, is from *Rhodospirillum rubrum*; and the phosphoribulokinase, which converts D-ribulose-5-phosphate to Ribulose-1,5-bisphosphate, is from *Spinacia oleracea*. The GroEL and GroES chaperonins of Rubisco are from *E. coli*. All these genes were codon-optimized by Sangon for expression in yeast, except for *FGH1*, *FLD1*, *AOX*, and *PYC1*.

Reagents and chemicals

Primers were synthesized by Sangon Biotech (China). PCR reactions were conducted using KOD FX201 DNA polymerases (Toyobo, Japan). Restriction enzymes and ligases for plasmid construction were obtained from New England Biolabs (USA). The assembly of multiple DNA fragments for plasmid construction was performed using the ClonExpress MultiS One-Step Cloning Kit (Vazyme Biotech, China). Plasmid isolation and DNA purification were performed using kits from Biomed Biotechnology Company Limited (China).

The methanol-^{13}C (Sigma-Aldrich, 277177-5G) and formic acid-^{13}C (Sigma-Aldrich, 279404-1G) were purchased from Sigma-Aldrich. The $NaH^{13}CO_3$ (Aldrich, S331496-1g) was purchased from Aldrich. The mass spectrometry-grade ammonium acetate, ammonium hydroxide, and acetonitrile were purchased from Sigma. Additional reagents, including analytical standards, were obtained from Sigma-Aldrich. All amino acids and vitamins were purchased from Sangon Biotech (Shanghai, China). The YNB (without amino acids and ammonium sulfate) was purchased from Thermofisher (Thermofisher, 233520). The DL-glyceraldehyde 3-phosphate (Aladdin, D347018-25mg) and dihydroxyacetone (Aladdin, D189238-100g) were purchased from Aladdin (USA).

Medium and growth conditions

CEN.PK2-1C and its mutants were typically cultured in yeast extract peptone dextrose (YPD) medium (20 g/L peptone, 20 g/L glucose, and 10 g/L yeast extract) or SC-Ura/His medium (1.7 g/L yeast nitrogen base (YNB) without amino acids and ammonium sulfate, 5 g/L ammonium sulfate, 20 g/L glucose, 0.77 g/L dropout mix (without uracil or histidine) contains all essential amino acids and nucleotides except uracil. *E. coli* strains were cultured in Luria-Bertani (LB) medium with 100 µg/mL ampicillin at 37 °C with shaking at 220 rpm. Solid media contained 15 g/L agar.

Methylotrophic growth evaluation was performed in the minimal medium (MM) supplemented with different carbon sources[20,23]. The modified MM consists of 7.5 g/L $(NH_4)_2SO_4$, 14.4 g/L KH_2PO_4, 2.1g/L K_2HPO_4, 0.5 g/L $MgSO_4·7H_2O$, 1 mL/L vitamin solution (0.05 g/L biotin, 0.2 g/L p-amino benzoic acid, 1 g/L nicotinic acid, 1 g/L calcium pantothenate, 1 g/L pyridoxine-HCl, 1 g/L thiamine-HCl, and 25 g/L myo-inositol 25 at pH 6.5) and 2 mL/L trace metal solution (15.0 g/L EDTA-Na_2, 4.5 g/L $ZnSO_4·7H_2O$, 0.84 g/L $MnCl_2·2H_2O$, 0.3 g/L $CoC1_2·6H_2O$, 0.3 g/L $CuSO_4·5H_2O$, 0.4 g/L $Na_2MoO_4·2H_2O$, 4.5 g/L $CaC1_2·2H_2O$, 3 g/L $FeSO_4·7H_2O$, 1 g/L H_3BO_3, and 0.1 g/L potassium iodide at pH 4.0, and amino acids (20 mg/L Uracil, 50 mg/L histidine, 100 mg/L tryptophan, 100 mg/L leucine, 100 mg/L lysine, 100 mg/L threonine, 50 mg/L serine, and 20 mg/L methionine).

To evaluate methylotrophic growth, engineered strains (triplicates) were pre-cultured in YPD medium or MM with 10 g/L methanol. Cells were washed twice with phosphate-buffered saline (PBS, pH 7.2) and inoculated into MM with 10 g/L or 20 g/L methanol at an OD_{600} of 0.05. Cultures were incubated at 30 °C for 2 to 8 days until reaching the exponential growth phase, then transferred to fresh methanol MM (OD_{600} of 0.05 or 0.10) for growth analysis. To minimize methanol evaporation during fermentation, the setup was sealed with a double layer of sterile, breathable filter membrane. The reported methanol consumption data have been corrected for evaporation losses, as determined by the control experiments detailed in Supplementary Fig. 21. Specific growth rate (μ) was calculated using Equation **1**. The maximum specific growth rate was calculated by fitting the OD_{600} measurements to a linear model during the exponential growth phase in methanol MM. Doubling time (*DT*) and generation number (*N*) were calculated using Equation **2** and **3**, respectively.

$$\mu = \frac{\ln(\mathrm{OD600}_{t2}) - \ln(\mathrm{OD600}_{t1})}{t2 - t1} \qquad (\mathbf{1})$$

$$DT = \frac{\ln(2)}{\mu} \qquad (\mathbf{2})$$

$$N = \frac{t}{\mathrm{DT}} \qquad (\mathbf{3})$$

All strains were cultivated in a shaking incubator (ZCZY-ASBES, Chichu Biotechnology (Shanghai) Co., Ltd., China) at 30 °C with a shaking speed of 180 rpm. Cell density was obtained by measuring the OD600 value using a spectrophotometer (DeNovix DS-11+, USA).

Cell-free extraction preparation and protein purification

Single colonies were picked from plates and inoculated into synthetic dropout medium with 20 g/L glucose. After overnight incubation, 100 µL of the culture was transferred to 100 mL synthetic drop-out medium with 20 g/L glucose and incubated at 30 °C with shaking at 180 rpm for 48 hours. The culture was then centrifuged at 14,000 × g for 1 minute at 4 °C and washed with 0.1 M potassium phosphate buffer (pH 7.2). The centrifugation was repeated under the same conditions. Finally, 20 mL of 0.1 M PBS (pH 7.2) and 500 µL of glass beads (0.40–0.45 mm) were added to the tubes with cell pellets. Cell-free extract was obtained using an ultrasonic disruptor (ScientZ-JY92-IIN) set to 300 W power and 60% amplitude, with 10 seconds of sonication followed by a 10-second pause, repeated six times. The samples were kept on ice during disruption. Cell debris was removed by centrifugation at 4,500 × g for 6 min at 4 °C. Proteins were purified using a His-tag column (Thermo Fisher, HisTrap HP) and Fast protein liquid chromatography (FPLC). Further details for protein purification are available in Supplementary Method 1.

Genetic manipulation

The primers used in this study, synthesized by Sangon Biotech (China), are listed in Supplementary Data 3. All gene sequences are in Supplementary Data 4. Expression cassettes (promoters, genes, and terminators) were amplified using the high-fidelity KOD FX201 DNA polymerase (Toyobo, Japan). Plasmid construction using two fragments was performed via digestion and ligation. Restriction enzymes and ligases were obtained from New England Biolabs (USA). Plasmid construction with multiple fragments was performed using the ClonExpress MultiS One-Step Cloning Kit (Vazyme Biotech, China). Plasmid isolation and DNA purification were carried out using kits from Biomed Biotechnology Company Limited (China). Genetic manipulation of CEN.PK2-1C was performed using the gRNA-tRNA array for CRISPR-Cas9 (GTR-CRISPR)[66]. All guide RNAs used in genomic manipulation were designed using the CRISPRdirect tool[67] and were summarized in Supplementary Table 3. All modified genotypes were confirmed by colony PCR and sequencing. Detailed protocols for gene editing and identification are available in Supplementary Method 2.

Enzymes activity assay

The Aox-Pyc1, Mdh3-Act1, Fld1, Fgh1, Fdh1, and Cat from SC-AOX$_0$, and the Rubisco-GroEL-GroES, Prk, ALD4, Tkl1, and Tkl2 from SC-AOX$_{25}$-CBB were expressed and purified based on the procedure outlined above. Activity of Aox was assessed through an *in vitro* methanol oxidation reaction, where 5 mg of purified Aox, 5 mM FAD, and 2.25 M methanol were added into 10 mM Dipotassium phosphate buffer (pH 7.2) to a total volume of 1 mL[68]. After one hour of incubation at 30 °C, the reaction was terminated by adding 0.1 mL of 2 M H_2SO_4. Formaldehyde was measured by adding 1.5 mL of Nash reagent[69] (Supplementary Fig. 22). The specific activity of Aox is defined as the amount of enzyme that produces 1 μmol of formaldehyde per minute. The calibration curve and specific activity calculations for formaldehyde are summarized in Supplementary Method 3.

Activity of Mdh3 with activator Act1 was assessed through an *in vitro* methanol oxidation reaction where 5 mg of purified Mdh3, 2 mL of 10% methanol, and 5 mM NAD^+ were added into 50 mM Dipotassium phosphate buffer (pH 7.2) supplemented with 5 mM $MgSO_4$ to a total volume of 1 mL[20]. After one hour at 30 ℃, the reaction was terminated by adding 0.1 mL of 2 M H_2SO_4. Formaldehyde production was quantified by adding 1.5 mL of Nash reagent[69]. The specific activity of Mdh3 is defined as the amount of enzyme that produces 1 μmol of formaldehyde per minute.

Activity of Fld1 was assessed through an *in vitro* formaldehyde oxidation reaction where 6 pmol of GSH, 3 pmol of NAD, 2.9 pmol of formaldehyde, and 5 mg of Fld1 were added into 100 pmol of sodium phosphate buffer (pH 8.0) to a total volume of 3 mL[70]. After 1 hour at 30 °C, the reaction was terminated. NADH production was quantified based on the fluorescence intensity at Ex/Em = 540/590 nm using a microplate reader (BioTek Synergy H1, USA). The specific activity of Fld1 is defined as the amount of enzyme that produces 1 μmol of NADH per minute. The calibration curve and specific activity calculations for NADH are summarized in Supplementary Method 3.

Esterase activity of the purified Fgh1 protein was assessed using *S*-acetylglutathione as the primary substrate. Hydrolysis was monitored spectrophotometrically at 240 nm[71]. For comparison, the hydrolysis rate of the reference substrate, 4-methylumbelliferyl acetate (4-MUA), was determined fluorometrically (excitation at 355 nm, emission at 480 nm). Calibration curves were generated using dilution series of *S*-acetylglutathione and 4-methylumbelliferone, respectively (Supplementary Fig. 23). The enzymatic reaction (250 μL total volume) was performed at 30 °C in 50 mM potassium phosphate buffer (pH 7.0), containing 2 mg of enzyme and one of the following substrates: 0.35 mM *S*-acetylglutathione or 0.3 mM 4-methylumbelliferyl acetate (4-MUA). One unit of Fgh1 activity (U) is defined as the amount of enzyme catalyzing the production of 1 μmol of product (glutathione or 4-methylumbelliferone) per minute. Protein concentration was quantified using the Bradford method[72] with a Bio-Rad protein assay kit, using bovine serum albumin as the standard. The calibration curve and specific activity calculations for Fgh1 are summarized in Supplementary Method 3.

Fdh1 activity was assessed through an *in vitro* formate oxidation reaction where 5 mg of purified Fdh1, 10 mM formate, and 2 mM NAD^+ were added into 50 mM Potassium phosphate buffer (pH 7.0) to a total volume of 1 mL[73]. After 1 hour at 30 °C, the reaction was terminated. NADH production was quantified as described for Fgh1 using the Fluorimetric NADH Assay Kit. The specific activity of Fdh1 is defined as the amount of enzyme that produces 1 μmol of NADH per minute.

Catalase activity was assessed through an *in vitro* hydrogen peroxide oxidation reaction, where 5 mg of purified Catalase and 10 mM Hydrogen peroxide (H_2O_2) were added into 5 mM phosphate buffer (pH 7.0) to a total volume of 10 mL[74]. After 10 min at 0 °C, the reaction was terminated by adding 2 mL of 2.0 N H_2SO_4 saturated with Titanium sulfate ($TiSO_4$). The H_2O_2 decomposition was monitored by absorbance at 410 nm using a microplate reader (BioTek Synergy H1, USA) (Supplementary Fig. 22). The specific activity of Cat is defined as the amount of enzyme that decomposes one mmol H_2O_2 per minute. The calibration curve and specific activity calculations for H_2O_2 are summarized in Supplementary Method 3.

Rubisco activity was assessed through an *in vitro* carboxylation reaction, where 5 mM Ribulose-1,5-bisphosphate, 5 mg purified Rubisco with its chaperone proteins GroEL and GroES, 1 mM ATP, 5 mM creatine phosphate, 20 mM $NaHCO_3$, 0.2 mM NADH, and 5 mg coupling enzymes (glyceraldehyde-3-phosphate dehydrogenase (Shanghai Yuanye Bio-Technology Co., Ltd), Phosphoglycerate kinase (Real-Times (Beijing) Biotechnology Co., Ltd), Triosephosphate isomerase and glycerol-3-phosphate dehydrogenase (Shanghai Yuanye Bio-Technology Co., Ltd) were added into the assay buffer (100 mM EPPS-NaOH, pH 8.0, 20 mM $MgCl_2$, 1 mM EDTA) to a total of 1 mL[52,75-77]. Purified Rubisco-chapron complex was pre-activated with 15 mM $MgCl_2$

and 15 mM $NaHCO_3$ for 10 min. After 1 hour at 30 °C, the reaction was terminated. Activity was measured spectrophotometrically by tracking the conversion of NADH to NAD^+. The specific activity of Rubisco is defined as the amount of enzyme that produces 2 μmol NAD^+ per minute (Supplementary Fig. 24).

Prk activity was assessed through an *in vitro* reaction, where 2.5 mM D-ribulose-5-phosphate, 40 mM KCl, 10 mM $MgCl_2 \cdot 6H_2O$, 0.15 mM NADH, 1 mM ATP, 3 mM phosphoenolpyruvate, 1 mM 1,4-Dithiothreitol, 5 U of pyruvate kinase (Sigma-Aldrich), 6 U of L-lactate dehydrogenase (Yuan Ye Co., China) were added into the 50 mM Tris–HCl (pH 8.2) to a total of 1 mL[53,78]. After 30 min at 30 °C, the reaction was terminated. NADH production was quantified as described for Fgh1. The specific activity of Prk is defined as the amount of enzyme that produces 1 μmol NADH per minute.

Activities of Tkl1 and Tkl2 were assessed through an *in vitro* reaction. The following components were combined in a total volume of 1 mL within 50 mM Tris–HCl buffer (pH 8.2): 50 μL of D-ribulose-5-phosphate (R5P, substrate, 20 mM), 4 mM thiamine pyrophosphate (TPP), 4 mg of purified enzyme, and 600 μL of 136 mM Tris-HCl (pH 7.8)[79]. After incubation at 37 °C for 2 hours, the reaction was terminated by adding an equal volume of methanol. The mixture was centrifuged, and the supernatant was collected, lyophilized, and reconstituted in 150 μL of 50% (v/v) methanol for mass spectrometry analysis. Products glyceraldehyde-3-phosphate (GAP) and dihydroxyacetone phosphate (DHA) were detected by Q-TOF MS (instrumental conditions as detailed in the ^{13}C metabolite tracer analysis methods).

Activity of Ald4 was measured in an *in vitro* assay[80]. Aldehyde dehydrogenase activity was determined at 30 °C using a microplate spectrophotometer (BioTek Synergy H1, USA). The reaction mixture for Ald4 contained a buffer composed of 50 mM HEPES-KOH (pH 7.5), 20 mM KCl, 0.4 mM NAD+, and 5 mM EDTA. Activity was quantified by monitoring the increase in absorbance due to NADH formation over time. One unit of specific activity for Ald4 is defined as the amount of enzyme required to produce 1 μmol of NADH per minute per milligram of protein.

Quantitative real-time-PCR

Three single cells of the SC-AOX$_0$, SC-AOX$_{25}$, and SC-AOX$_{25}$-CBB were pre-cultured in MM with 10 g/L methanol (SC-AOX$_{25}$ and SC-AOX$_{25}$-CBB) or 20 g/L glucose (SC-AOX$_0$) at 30 °C with shaking 180 rpm in a 40 mL volume within a 250 mL bottle. Cells were washed twice with PBS (pH 7.2). The resulting cells were then inoculated in MM with 10 g/L methanol (SC-AOX$_{25}$ and SC-AOX$_{25}$-CBB) or 20 g/L glucose (SC-AOX$_0$) at an OD$_{600}$ of 0.05 and cultured at 30 °C for 2 to 8 days until they reached the exponential growth phase. Total RNA was isolated from cells in the logarithmic growth phase using TRNzol Reagent (Sangon Biotech, Shanghai, China). cDNA synthesis was performed using the PrimeScript™ RT reagent Kit with gDNA Eraser (TaKaRa, Japan). Quantitative real-time PCR (qRT-PCR) was performed on the Applied Biosystems 7500 Fast Dx Real-Time PCR system (Applied Biosystems, USA). Analysis, including standard curve construction, expression normalization, and calculation of standard error values, was conducted using the Eco Real-Time PCR System Software (Illumina) and the $2^{-\Delta\Delta CT}$ method[81]. The *ALG9* gene served as a normalization control[82]. Verification of qRT-PCR products was performed through melting curve analysis and peak identification. Primers used for real-time PCR are summarized in Supplementary Data 3, and details of calculations and measurements are provided in Supplementary Method 4.

Adaptive laboratory evolution

Adaptive laboratory evolution (ALE) was performed on SC-AOX$_0$, SC-MDH$_0$, and CEN.PK2-1C in MM with methanol using serial transfers in shake flasks. The process consisted of stages: initial screening for methanol growth and selecting tolerated and fast-growing mutants (Supplementary Fig. 3). Cells from three independent colonies were cultured in YPD medium at 30 °C and 180 rpm, overnight in baffled shake flasks (40 mL). Log-phase cells were washed three times with

MM, transferred to 40 mL of MM with 10 g/L methanol, and cultured at 30 °C, 180 rpm. After 8 days, cells were washed and transferred to fresh MM with 10 g/L methanol. This cycle was repeated until the mutants capable of growth were selected. Selection was conducted in a 96-well plate (BioTek Synergy H1, USA). In the second stage, the strains growing on 20 g/L methanol were screened. Yeast strains were cultured in YPD, washed with MM with methanol, and transferred to MM with 20 g/L methanol. After 4 days, the specific growth rates were recorded, and cells were washed and transferred repeatedly. This continued until fast-growing strains were selected in a 96-well plate. ALE concluded upon achieving a stable growth rate in MM with 20 g/L methanol.

The single-colon cells from the evolved pools were obtained using a flow cytometer (CytoFLEX SRT-1, Beckman, USA). The evolved pools were cultured in MM with 20 g/L methanol for 4 days (late log phase), and then the cells were collected. All cells were stained with CFDA-AM dye and propidium iodide (PI). *S. cerevisiae* cells with intact cell membranes stain fluorescent green (FITC B525-A), whereas cells with damaged membranes stain fluorescent red (PE Y585-A). The cells were divided into three sections: Q1-UL, standard non-vitally compromised cells; Q1-UR, standard vitally compromised cells; Q1-LR, standard vitally intact cells. Cells from Q1-LR were sorted for further analysis. The detailed process of flow cytometry is provided in Supplementary Method 5.

^{13}C metabolite tracer analysis

The methods of the ^{13}C metabolite tracer analysis were modified from the previous study[20]. In brief, for the analysis of ^{13}C-labeled amino acids and metabolites within the central metabolic pathway, SC-AOX$_{25}$ was first cultured in MM with 10 g/L of unlabeled methanol as the carbon source for approximately 72 hours, reaching the exponential growth phase. The cells were washed twice with PBS (pH 7.2) and then transferred to MM with 10 g/L ^{13}C-labeled methanol at an OD$_{600}$ of 0.05, where they were incubated until the exponential growth phase was reached. The resulting cell culture was washed with PBS and then incubated in fresh MM containing 10 g/L ^{13}C-labeled methanol until it entered the exponential growth phase again. This process was repeated for three generations. The 4th generation of cells incubated with ^{13}C-MeOH ($OD_{600} \approx 0.53$) was pelleted by centrifugation at 8,000 × g and 4 °C for 3 min. The cells were then resuspended in a cold mixture of 300 µL methanol at −20 °C, 300 µL chloroform at −20 °C, and 250 µL water at 4 °C. After vortexing, the supernatant was transferred to a pre-cooled 1.7 mL screw-cap tube, and 500 µL of pre-cooled glass beads were added. Cell lysis was performed using a homogenizer (SCIENTZ-48LT, SCIENTZ Co., China) at 70 Hz, oscillating for 30 seconds with 15-second intervals at a temperature of 4 °C. The lysed cells were centrifuged at 10,000 × g and 4 °C for 10 min. The supernatant was flash-frozen in liquid nitrogen and lyophilized. Finally, the samples were reconstituted in 50 µL of a 50:50 methanol-water mixture for analysis.

Analysis was conducted using an LC-MS system comprising an Agilent 1290 Infinity II UHPLC system in tandem with timsTOF Pro2 (Bruker). Extracted metabolites were dissolved in 100 uL of 50% methanol for analysis. Chromatographic separation was achieved on an ACQUITY UPLC BEH Amide column (100 mm × 2.1 mm, 1.7 µm). The mobile phase A consisted of 15 mM ammonium acetate, 0.3% $NH_3 \cdot H_2O$ in water, and the mobile phase B consisted of 15 mM ammonium acetate, 0.3% $NH_3 \cdot H_2O$ in 9:1 (v/v) acetonitrile/water. The flow rate was 0.3 mL/min. The column was washed with 95% mobile phase B for 1 minute, followed by a linear gradient to 50% over 8 min, held at 50% for 3 min, then a linear gradient back to 95% over 0.5 min, with a final 1.5 min at 95%. A total of 5 µL sample was injected for each analysis.

For ^{13}C-formate and $^{13}CO_2$ experiments, the MM lacking serine and glycine, supplemented with 10 g/L of unlabeled methanol, was used to provide either 5 g/L of ^{13}C-formate or 0.01 M $NaH^{13}CO_3$, respectively. Other sample preparation and analysis methods were identical to those used in the ^{13}C-MeOH experiments. For all ^{13}C-labeled experiments, samples prepared with MM or MM without serine and glycine, supplemented with unlabeled formate, methanol, or $NaHCO_3$, were used as negative controls. All final ^{13}C incorporation data were corrected for natural isotopic abundance using the AccuCor2 algorithm of Bruker TASQ software[83]. The specific ^{13}C incorporation was calculated based on Equation **4**.

$$FC = \frac{\sum_{i=0}^{n} i \cdot s_i}{n} \qquad \textbf{(4)}$$

n represents the number of carbon atoms in the metabolite and *Si* denotes the relative fraction of each isotopologue. Fractional contribution (*FC*) represents the average carbon labeling, which quantifies the mean percentage of isotopic labeling (e.g., ^{13}C incorporation) per carbon atom in a metabolite[83]. Corrected isotopologue abundance represents the natural isotope abundance-corrected relative abundance (S_i) of a specific isotopologue (e.g., M+1, M+2), expressed as a percentage[83]. Representative labeling patterns for glucose-6-phosphate are presented in Supplementary Fig. 25.

Whole-genome sequencing and data analysis

Whole-genome sequencing of the evolved strains SC-AOX$_9$ and SC-AOX$_{25}$ was conducted after culturing in MM with 10 g/L methanol. High-quality genomic DNA extracted using the CTAB method[84] underwent rigorous quality assessment, including agarose gel electrophoresis and NanoDrop quantification. Sequencing libraries were prepared using Illumina TruSeq or PacBio SMRTbell kits, followed by sequencing on Illumina NovaSeq X Plus or PacBio long-read platforms. Raw reads were processed to remove low-quality sequences, aligned to the reference genome (NCBI accession: GCA_002885995.1), and analyzed for germline/somatic variants (SNPs, INDELs), structural variations (SVs), and copy number variations (CNVs) using BWA-MEME, Sentieon Genomics Tools, Manta, CNVkit, Sniffles, and HiFiCNV[85]. Variants were functionally annotated with SnpEff[86]. Details of processes are provided in Supplementary Method 6.

Transcriptome profiling

Biological triplicates of strains SC-AOX$_0$, SC-AOX$_9$, and SC-AOX$_{25}$ were cultured in MM supplemented with 10 g/L methanol (SC-AOX$_9$ and SC-AOX$_{25}$) or 20 g/L glucose (SC-AOX$_0$ as a control). Cells were harvested during the logarithmic phase (OD$_{600}$ ≈ 0.53), flash-frozen, and subjected to total RNA extraction using TRIzol®. High-quality RNA (OD$_{260/280}$ = 1.8–2.2, OD$_{260/230}$ ≥ 2.0, RQN ≥ 6.5, 28S:18S ≥ 1.0) was used for library preparation with the Illumina® Stranded mRNA library Prep Kit, including polyA selection, fragmentation, double-stranded cDNA synthesis, end repair, adapter ligation, and PCR amplification. Libraries were sequenced on an Illumina Nova Seq X Plus platform (paired-end 150 bp reads). Raw reads were processed with Fastp for quality trimming, aligned to the reference *S. cerevisiae* CEN.PK113-7D reference genome (https://www.ncbi.nlm.nih.gov/datasets/genome/GCA_002885995.1/) using HISAT2, and assembled with StringTie[87]. Differential expression analysis ($|\log2FC| \geq 1$, FDR < 0.05/0.001) was performed using DESeq2/DEGseq, followed by GO/KEGG pathway enrichment (Bonferroni-corrected $P < 0.05$) and alternative splicing analysis with rMATS[88]. Details protocols are provided in Supplementary Method 7.

Methanol, formate, and formaldehyde detection

Cells were cultured in YPD or MM at 30 °C with vigorous shaking (180 rpm), harvested by centrifugation (10,000 × g, 10 min), washed twice with PBS, and resuspended in MM with 10 g/L methanol (initial OD$_{600}$ = 0.05). At designated time points, 500 µL aliquots were collected and centrifuged (10,000 × g, 4 °C, 10 min). Supernatants were analyzed using an Agilent 1260 HPLC system (USA) equipped with a Bio-Rad Aminex HPX-87H column (300 mm × 7.8 mm, 5 µm particle size) maintained at 60 °C. The mobile phase consisted of 5 mM H_2SO_4 at a flow rate of 0.6 mL/min. Formate and pyruvate were quantified by UV detection at 210 nm, while methanol was measured via refractive index detection (RID, Agilent G1362A). Detailed protocols are provided in Supplementary Method 8.

Formaldehyde was quantified using either a commercial assay kit (Abcam Formaldehyde Assay kit, England; Catalog No. 272524) or Nash reagent[89]. Strains SC-AOX$_9$ and SC-AOX$_{25}$ were precultured in MM with 10 g/L methanol (initial OD_{600} = 0.05), harvested after 72 h, and lysed in PBS (pH 7.2) via mechanical homogenization with 0.5 mm glass beads (70 Hz, 30 s pulses, 4 °C). Lysates were centrifuged at 10,000 × g for 10 min at 4 °C, and supernatants were deproteinized with 10% trichloroacetic acid. For the kit-based assay, fluorescence intensity was measured at excitation/emission wavelengths of 370/470 nm after 30 min incubation at room temperature. For Nash reagent detection, samples were mixed with Nash reagent (5M ammonium acetate, 50 mM Acetylacetone) and incubated at 37 °C for 1 h. Absorbance at 412 nm was recorded using a BioTek Synergy H1 microplate reader (Agilent, USA). Detailed protocols are provided in Supplementary Method 8.

Intracellular ATP and NADH assay

The detection of ATP was developed based KeyTec® Luminescent Cell Viability Detection Kit (Key Scientific, Catalog number A2010002N, USA) with slight modifications[90]. The principle is based on a luminescent system developed for cell viability analysis, where the number of metabolically active live cells is determined by quantitatively measuring ATP content after cell lysis[90]. Biological triplicates of engineered variants were pre-cultured in MM with 10 g/L methanol and then inoculated into fresh MM containing either 10 g/L methanol or 10 g/L methanol plus 20 g/L glucose. Cells were collected during the exponential phase, with those cultured in MM containing 20 g/L glucose serving as the control. For cell lysis, cells were resuspended in 600 µL of sterile double-distilled water in a sterile tube, followed by the addition of 250 µL of pre-cooled glass beads (0.5 mm diameter). Mechanical disruption was performed using a SCIENTZ-48LT homogenizer (SCIENTZ Co., China) at 70 Hz with 30-second oscillations (15-second intervals) at 4 °C. The reaction mixture was prepared by adding 100 µL of LCV (Luminescent Cell Viability) reagent to 100 µL of lysate in a white 96-well plate, followed by shaking for 2 min to ensure thorough mixing and a 10-minute reaction at room temperature. Luminescent signals were recorded using a BioTek Synergy H1 microplate reader (Agilent, USA) with kinetic measurements over a 30-minute period. The ATP standard curve is shown in Supplementary Fig. 26.

The detection of NADH was performed according to methods described in previous study[91]. Briefly, the principle relies on the Amplite NADH Assay Kit (AAT Bioquest, USA), which employs an enzyme cycling reaction to specifically detect and amplify the NADH signal, thereby enhancing sensitivity[91]. Cells were cultured and collected using the same protocol as described above for the ATP detection. Briefly, 50 μL of NADH standards or test samples were placed in a black 96-well plate. The mixture was incubated at room temperature for 1 hour (protected from light), and fluorescence intensity was recorded at excitation/emission wavelengths of 540 nm and 590 nm, respectively, using a BioTek Synergy H1 microplate reader (Agilent, USA) with kinetic measurements over 30 minutes. The NADH standard curve (Supplementary Fig. 26) was generated using serial dilutions of NADH.

Scanning electron microscope

The SC-AOX$_{25}$, SC-AOX$_9$, SC-AOX$_0$, and CEN.PK2-1C strains were subjected to scanning electron microscope (SEM) analysis using the method reported in previous study[20]. In brief, all strains were pre-cultured in MM supplemented with 10 g/L methanol and then re-included in the same medium for an additional 4 days until the medium turned dark green (indicating the logarithmic phase), followed by SEM preparation. Cells were collected and processed according to the detailed fixation, acid treatment, and dehydration methods outlined in Supplementary Method 9. They were then observed at various magnifications (1 μm, 2 μm, 3 μm, and 5 μm) using a Regulus 8230 field emission scanning electron microscope (Hitachi, Japan).

Isolation of the DNA-protein crosslinking complexes and TEM analysis

The extraction of DNA-protein crosslinking complexes was based on previous study[17]. SC-AOX$_{25}$ was cultured in MM supplemented with 10 g/L or 20 g/L methanol at an initial OD$_{600}$ of 0.05. Cells were harvested during three growth phases: exponential, stationary, and late phase. Cell pellets were obtained by centrifuging three 40 mL cultures at 5,000 × g for 5 min, then resuspended in lysing buffer (10 mM MOPS) containing lysozyme (50 U/mL) at 30 °C for 60 min. DNA was extracted using DNAzol reagent[17], precipitated with ethanol at -80 °C for ≥ 1 h, and dissolved in 8 mM NaOH. Proteins were removed by treatment with Tris-HCl (pH 7.4), 8 M urea, and 2% SDS (w/v) at 37 °C for 30 min. The sample underwent salting-out with 5 M NaCl, ultrafiltration using a 3 kDa cut-off membrane, and ethanol precipitation with 0.3 M potassium acetate. DNA was washed with 70% ethanol, dissolved in Tris-EDTA buffer (10 mM), and quantified by spectrophotometry at 260 nm. Details are provided in Supplementary Method 10.

Transmission electron microscopy (TEM) was performed as follows. Approximately 500 ng of purified DPC complexes were mounted onto activated 300-mesh copper grids (carbon-stabilized form, Ted Pella) for 1 min at room temperature. Excess liquid was blotted with filter paper, and samples were stained with 2.5% uranyl acetate for 1 min. After air-drying, samples were imaged using a Talos L120C G2 transmission electron microscope (Thermo Fisher Scientific) operated at 120 kV. Detailed procedures are provided in Supplementary Method 10.

Protein sample preparation for quantitative proteomics and LC-MS/MS analysis

To analyze the DPC complexes, the protein portion was purified and processed for quantitative proteomics as described in previous studies[17,92,93]. In brief, extracted DNA cross-links were incubated at 70 °C for 1 hour, then treated with 1 µL each of DNase I (NEB) and S1 nuclease (Thermo Fisher Scientific) to remove DNA. The resulting small DNA fragments were filtered using a 3 kDa Amicon Ultra-0.5 mL centrifugal filter, and the sample was concentrated to 50 µL via centrifugation. Protein concentration was measured at 280 nm using a Nanodrop spectrophotometer. Proteins were separated on 12% SDS-PAGE gels (Bio-Rad) and visualized by silver staining with the Pierce Silver Staining Kit (Thermo Fisher Scientific).

The protein samples were then prepared for quantitative proteomics and LC-MS/MS analysis. The decrosslinked samples were denatured with 4 M urea and reduced with 10 mM dithioerythritol

(DTT) at 37 °C for 45 minutes. Subsequently, proteins were alkylated with 25 mM iodoacetamide in the dark at room temperature for 1 hour. Digestion was performed overnight at 37 °C using LysC and trypsin at an enzyme-to-substrate ratio of 1:50 (w/w). The resulting peptides were desalted using a C18 StageTip prior to LC-MS/MS analysis.

For LC-MS/MS analysis, lyophilized peptides were resuspended in 0.1% formic acid (16 µL) and analyzed on a nanoElute UHPLC system (Bruker) coupled to a timsTOF HT mass spectrometer (Bruker Daltonics). Peptides were ionized using a CaptiveSpray nano-electrospray source and separated on a 25 cm × 75 µm C18 column (IonOpticks Aurora series) with a 30-minute gradient of 4-80% acetonitrile/0.1% formic acid at 300 nL/min. The mass spectrometer was operated in DDA-PASEF mode with an *m/z* range of 300 to 1500 and ion mobility compensation (K_0) ranging from 0.75 to 1.3. Label-free quantification was performed using MSFragger (FragPipe v20.0) with the LFQ-MBR workflow, applying a 20 ppm mass tolerance, 3-minute retention time window, 0.05 ion mobility tolerance, and a 1% FDR (false discovery) peptide filter. No normalization was applied, and a minimum isotope count of 2 was required for data reliability. Details are provided in Supplementary Method 10.

Data availability

The RNA-seq data and genome resequencing data generated in this study have been deposited in the NCBI SRA database under Bioproject PRJNA1238490 [https://www.ncbi.nlm.nih.gov/bioproject/?term=PRJNA1238490] and PRJNA1238044 [https://www.ncbi.nlm.nih.gov/bioproject/?term=PRJNA1238044], respectively. The proteomics data have been deposited in the ProteomeXchange Consortium via the PRIDE repository under accession PXD064258 [https://www.ebi.ac.uk/pride/archive/projects/PXD064258] and PXD064984 [https://www.ebi.ac.uk/pride/archive/projects/PXD064984]. Source data are provided with this paper.

Declaration of generative AI and AI-ASSISTED technologies

During the preparation of this manuscript, the authors utilized Grammarly (https://www.grammarly.com/) and DeepSeek (www.deepseek.com) for grammatical revision and language polishing. All AI-generated suggestions were critically reviewed and manually adjusted by the authors, who assume full responsibility for the intellectual content and academic integrity of this work.

References

1 Boehm, S. et al. State of Climate Action 2023. *World Resour. Inst* https://www.wri.org/research/state-climate-action-2023 (2023).

2 Sollai, S., Porcu, A., Tola, V., Ferrara, F. & Pettinau, A. Renewable methanol production from green hydrogen and captured CO_2: A techno-economic assessment. *J. CO2 Util*. **68**, 102345 (2023).

3 Meunier, N., Chauvy, R., Mouhoubi, S., Thomas, D. & De Weireld, G. Alternative production of methanol from industrial CO_2. *Renew. Energ*. **146**, 1192-1203 (2020).

4 Kelso, P. A., Chow, L. K. M., Carpenter, A. C., Paulsen, I. T. & Williams, T. C. Toward methanol-based biomanufacturing: Emerging strategies for engineering synthetic methylotrophy in *Saccharomyces cerevisiae*. *ACS Synth. Biol*. **11**, 2548-2563 (2022).

5 Bertau, M., Offermanns, H., Plass, L., Schmidt, F. & Wernicke, H.-J. *Methanol: The Basic Chemical and Energy Feedstock of the Future* Vol. 1 (Springer, 2014).

6 Patel, S. K. S. et al. Hierarchical macroporous particles for efficient whole-cell immobilization: Application in bioconversion of greenhouse gases to methanol. *ACS Appl. Mater. Interfaces* **11**, 18968-18977 (2019).

7 Bennett, R. K., Steinberg, L. M., Chen, W. & Papoutsakis, E. T. Engineering the bioconversion of methane and methanol to fuels and chemicals in native and synthetic methylotrophs. *Curr. Opin. Biotechnol*. **50**, 81-93 (2018).

8 Ochsner, A. M., Sonntag, F., Buchhaupt, M., Schrader, J. & Vorholt, J. A. Methylobacterium

extorquens: methylotrophy and biotechnological applications. *Appl. Microbiol. Biotechnol*. **99**, 517-534 (2015).

9 Mo, X.-H. et al. Establishment of CRISPR interference in *Methylorubrum extorquens* and application of rapidly mining a new phytoene desaturase involved in carotenoid biosynthesis. *Appl. Microbiol. Biotechnol*. **104**, 4515-4532 (2020).

10 Schultenkämper, K., Brito, L. F., López, M. G., Brautaset, T. & Wendisch, V. F. Establishment and application of CRISPR interference to affect sporulation, hydrogen peroxide detoxification, and mannitol catabolism in the methylotrophic thermophile *Bacillus methanolicus*. *Appl. Microbiol. Biotechnol*. **103**, 5879-5889 (2019).

11 Yang, X., Zheng, Z. & Wang, Y. *Bacillus methanolicus*: an emerging chassis for low-carbon biomanufacturing. *Trends. Biotechnol*. **43**, 274-277 (2025).

12 Gao, J., Gao, N., Zhai, X. & Zhou, Y. J. Recombination machinery engineering for precise genome editing in methylotrophic yeast *Ogataea polymorpha*. *iScience* **24**, 102168 (2021).

13 Wang, L. et al. Efficient CRISPR–Cas9 mediated multiplex genome editing in yeasts. *Biotechnol. Biofuels* **11**, 277 (2018).

14 Liu, Q. et al. CRISPR–Cas9-mediated genomic multiloci integration in *Pichia pastoris*. *Microb. Cell Fact*. **18**, 144 (2019).

15 Guo, F., Qiao, Y., Xin, F., Zhang, W. & Jiang, M. Bioconversion of C1 feedstocks for chemical production using *Pichia pastoris*. *Trends. Biotechnol*. **41**, 1066-1079 (2023).

16 Cai, P., Gao, J. & Zhou, Y. CRISPR-mediated genome editing in non-conventional yeasts for biotechnological applications. *Microb. Cell Fact*. **18**, 63 (2019).

17 Chen, F. Y. H., Jung, H.-W., Tsuei, C.-Y. & Liao, J. C. Converting *Escherichia coli* to a synthetic methylotroph growing solely on methanol. *Cell* **182**, 933-946.e914 (2020).

18 Nieh, L.-Y. et al. Evolutionary engineering of methylotrophic *E. coli* enables fast growth on methanol. *Nat. Commun*. **15**, 8840 (2024).

19 Reiter, M. A. et al. A synthetic methylotrophic *Escherichia coli* as a chassis for bioproduction from methanol. *Nat. Catal*. **7**, 560-573 (2024).

20 Zhan, C. et al. Reprogramming methanol utilization pathways to convert *Saccharomyces cerevisiae* to a synthetic methylotroph. *Nat. Catal*. **6**, 435-450 (2023).

21 Guo, Y. et al. Engineering yeasts to co-utilize methanol or formate coupled with CO_2 fixation. *Metab. Eng*. **84**, 1-12 (2024).

22 Espinosa, M. I. et al. Adaptive laboratory evolution of native methanol assimilation in *Saccharomyces cerevisiae*. *Nat. Commun*. **11**, 5564 (2020).

23 Guo, F. et al. Evolutionary engineering of *Saccharomyces cerevisiae*: Crafting a synthetic methylotroph via self-reprogramming. *Sci. Adv*. **10**, eadq3484 (2024).

24 Attfield, P. V. Stress tolerance: The key to effective strains of industrial baker's yeast. *Nat. Biotechnol*. **15**, 1351-1357 (1997).

25 Nielsen, J. Yeast systems biology: Model organism and cell factory. *Biotechnol. J*. **14**, 1800421 (2019).

26 Lourens-Hattingh, A. & Viljoen, B. C. Growth and survival of a probiotic yeast in dairy products. *Food Res. Int*. **34**, 791-796 (2001).

27 Espinosa, M. I., Williams, T. C., Pretorius, I. S. & Paulsen, I. T. Benchmarking two *Saccharomyces cerevisiae* laboratory strains for growth and transcriptional response to methanol. *Syn. Syst. Biotechnol*. **4**, 180-188 (2019).

28 Dai, Z. et al. Metabolic construction strategies for direct methanol utilization in *Saccharomyces cerevisiae*. *Bioresour. Technol*. **245**, 1407-1412 (2017).

29 Lunt, S. Y. & Vander Heiden, M. G. Aerobic glycolysis: Meeting the metabolic requirements of cell proliferation. *Annu. Rev. Cell Dev. Bi*. **27**, 441-464 (2011).

30 Lieven, C., Herrgård, M. J. & Sonnenschein, N. Microbial methylotrophic metabolism: Recent metabolic modeling efforts and their applications in industrial biotechnology. *Biotechnol. J.* **13**, 1800011 (2018).

31 Liu, Z., Wang, K., Chen, Y., Tan, T. & Nielsen, J. Third-generation biorefineries as the means to produce fuels and chemicals from CO_2. *Nat. Catal*. **3**, 274-288 (2020).

32 Gregory, G. J., Bennett, R. K. & Papoutsakis, E. T. Recent advances toward the bioconversion

of methane and methanol in synthetic methylotrophs. *Metab. Eng*. **71**, 99-116 (2022).

33 Kim, S. et al. Growth of *E. coli* on formate and methanol via the reductive glycine pathway. *Nat. Chem. Biol*. **16**, 538-545 (2020).

34 Yu, H. & Liao, J. C. A modified serine cycle in *Escherichia coli* coverts methanol and CO_2 to two-carbon compounds. *Nat. Commun*. **9**, 3992 (2018).

35 He, H., Höper, R., Dodenhöft, M., Marlière, P. & Bar-Even, A. An optimized methanol assimilation pathway relying on promiscuous formaldehyde-condensing aldolases in *E. coli*. *Metab. Eng*. **60**, 1-13 (2020).

36 Wenk, S. et al. Evolution-assisted engineering of *E. coli* enables growth on formic acid at ambient CO_2 via the serine threonine cycle. *Metab. Eng*. **88**, 14-24 (2025).

37 Klein, V. J., Irla, M., Gil López, M., Brautaset, T. & Fernandes Brito, L. Unravelling formaldehyde metabolism in bacteria: Road towards synthetic methylotrophy. *Microorganisms* **10**, 220 (2022).

38 Moioli, E., Mutschler, R. & Züttel, A. Renewable energy storage via CO_2 and H_2 conversion to methane and methanol: Assessment for small scale applications. *Renew. Sust. Enegr. Rev*. **107**, 497-506 (2019).

39 Zhu, Z., Kin Tam, T., Sun, F., You, C. & Percival Zhang, Y. H. A high-energy-density sugar biobattery based on a synthetic enzymatic pathway. *Nat. Commun*. **5**, 3026 (2014).

40 Ullah, A., Hashim, N. A., Rabuni, M. F. & Mohd Junaidi, M. U. A review on methanol as a clean energy carrier: Roles of zeolite in improving production efficiency. *Energies* **16**, 1482 (2023).

41 Ozimek, P., Kötter, P., Veenhuis, M. & van der Klei, I. J. *Hansenula polymorpha* and *Saccharomyces cerevisiae* Pex5p's recognize different, independent peroxisomal targeting signals in alcohol oxidase. *FEBS Lett*. **580**, 46-50 (2006).

42 Zhong, W., Li, H. & Wang, Y. Design and construction of artificial biological systems for one-carbon utilization. *BioDes. Res*. **5**, 0021 (2023).

43 Flamholz, A., Noor, E., Bar-Even, A. & Milo, R. eQuilibrator-the biochemical

thermodynamics calculator. *Nucleic Acids Res*. **40**, D770-D775 (2012).

44 Beber, M. E. et al. eQuilibrator 3.0: a database solution for thermodynamic constant estimation. *Nucleic Acids Res*. **50**, D603-D609 (2022).

45 Sundström, M., Lindqvist, Y., Schneider, G., Hellman, U. & Ronne, H. Yeast *TKL1* gene encodes a transketolase that is required for efficient glycolysis and biosynthesis of aromatic amino acids. *J. Biol. Chem*. **268**, 24346-24352 (1993).

46 Navarro-Aviño, J. P., Prasad, R., Miralles, V. J., Benito, R. M. & Serrano, R. A proposal for nomenclature of aldehyde dehydrogenases in *Saccharomyces cerevisiae* and characterization of the stress-inducible *ALD2* and *ALD3* genes. *Yeast* **15**, 829-842 (1999).

47 Ruiz-Amil, M., de Torrontegui, G., Palacián, E., Catalina, L. & Losada, M. Properties and function of yeast pyruvate carboxylase. *J. Biol. Chem*. **240**, 3485-3492 (1965).

48 Qin, N. et al. Increased CO_2 fixation enables high carbon-yield production of 3-hydroxypropionic acid in yeast. *Nat. Commun*. **15**, 1591 (2024).

49 Chandel, N. S. Glycolysis. *Cold Spring Harb. Perspect. Biol.* **13**, *a040535* (2021).

50 Kresnowati, M. T. A. P. et al. When transcriptome meets metabolome: fast cellular responses of yeast to sudden relief of glucose limitation. *Mol. Syst. Biol*. **2**, 49 (2006).

51 Byrne, K. P. & Wolfe, K. H. The yeast gene order browser: Combining curated homology and syntenic context reveals gene fate in polyploid species. *Genome Res*. **15**, 1456-1461 (2005).

52 Xia, P. F. et al. Recycling carbon dioxide during xylose fermentation by engineered *Saccharomyces cerevisiae*. *ACS Synth. Biol*. **6**, 276-283 (2017).

53 Papapetridis, I. et al. Optimizing anaerobic growth rate and fermentation kinetics in *Saccharomyces cerevisiae* strains expressing Calvin-cycle enzymes for improved ethanol yield. *Biotechnol. Biofuels* **11**, 17-17 (2018).

54 Yasokawa, D. et al. Toxicity of methanol and formaldehyde towards *Saccharomyces cerevisiae* as assessed by DNA microarray analysis. *Appl. Biochem. Biotech*. **160**, 1685-1698 (2010).

55 Stingele, J. & Jentsch, S. DNA–protein crosslink repair. *Nat. Rev. Mol. Cell Bio*. **16**, 455-460 (2015).

56 Falcone, C. & Mazzoni, C. External and internal triggers of cell death in yeast. *Cell. Mol. Life Sci*. **73**, 2237-2250 (2016).

57 Carmona-Gutierrez, D. et al. Apoptosis in yeast: triggers, pathways, subroutines. *Cell Death Differ*. **17**, 763-773 (2010).

58 Spégel, C. F. et al. Amperometric response from the glycolytic versus the pentose phosphate pathway in *Saccharomyces cerevisiae* cells. *Anal. Chem*. **79**, 8919-8926 (2007).

59 Lu, X. et al. Constructing a synthetic pathway for acetyl-coenzyme a from one-carbon through enzyme design. *Nat. Commun*. **10**, 1378 (2019).

60 Mao, Y. F. et al. Non-natural aldol reactions enable the design and construction of novel one-carbon assimilation pathways *in vitro*. *Front. Microbiol*. **12**, 677596 (2021).

61 Nattermann, M. et al. Engineering a new-to-nature cascade for phosphate-dependent formate to formaldehyde conversion *in vitro* and *in vivo*. *Nat. Commun*. **14**, 2682 (2023).

62 Henras, A. K., Plisson-Chastang, C., O'Donohue, M.-F., Chakraborty, A. & Gleizes, P.-E. An overview of pre-ribosomal RNA processing in eukaryotes. *WIREs RNA* **6**, 225-242 (2015).

63 Nomura, M. Ribosomal RNA genes, RNA polymerases, nucleolar structures, and synthesis of rRNA in the yeast *Saccharomyces cerevisiae*. *Cold Spring Harb. Symp. Quant. Biol*. **66**, 555-565 (2001).

64 Berger, K. H. & Yaffe, M. P. Mitochondrial DNA inheritance in *Saccharomyces cerevisiae*. *Trends Microbiol*. **8**, 508-513 (2000).

65 de Zamaroczy, M. & Bernardi, G. The primary structure of the mitochondrial genome of *Saccharomyces cerevisiae* - a review. *Gene* **47**, 155-177 (1986).

66 Zhang, Y. et al. A gRNA-tRNA array for CRISPR-Cas9 based rapid multiplexed genome editing in *Saccharomyces cerevisiae*. *Nat. Commun*. **10**, 1053 (2019).

67 Naito, Y., Hino, K., Bono, H. & Ui-Tei, K. CRISPRdirect: software for designing CRISPR/Cas guide RNA with reduced off-target sites. *Bioinformatics* **31**, 1120-1123 (2015).

68 Evers, M. E., Harder, W. & Veenhuis, M. *In vitro* dissociation and re-assembly of peroxisomal alcohol oxidases of *Hansenula polymorpha* and *Pichia pastoris*. *FEBS Lett*. **368**, 293-296

(1995).

69 Couderc, R. & Baratti, J. Oxidation of methanol by the yeast, *Pichia pastoris*. purification and properties of the alcohol oxidase. *Agric. Biol. Chem*. **44**, 2279-2289 (1980).

70 SchÜTte, H., Flossdorf, J., Sahm, H. & Kula, M.-R. Purification and properties of formaldehyde dehydrogenase and formate dehydrogenase from *Candida boidinii*. *Eur. J. Biochem*. **62**, 151-160 (1976).

71 Degrassi, G., Uotila, L., Klima, R. & Venturi, V. Purification and properties of an esterase from the yeast *Saccharomyces cerevisiae* and identification of the encoding gene. *Appl. Environ. Microbiol*. **65**, 3470-3472 (1999).

72 Bradford, M. M. A rapid and sensitive method for the quantitation of microgram quantities of protein utilizing the principle of protein-dye binding. *Anal. Biochem*. **72**, 248-254 (1976).

73 Overkamp, K. M. et al. Functional analysis of structural genes for NAD^+-dependent formate dehydrogenase in *Saccharomyces cerevisiae*. *Yeast* **19**, 509-520 (2002).

74 Seah, T. C. M. & Kaplan, J. G. Purification and properties of the catalase of bakers' yeast. *J. Biol. Chem*. **248**, 2889-2893 (1973).

75 Ruuska, S. A., Badger, M. R., Andrews, T. J. & von Caemmerer, S. Photosynthetic electron sinks in transgenic tobacco with reduced amounts of Rubisco: little evidence for significant Mehler reaction. *J. Exp. Bot*. **51**, 357-368 (2000).

76 Yamori, W. & von Caemmerer, S. Effect of Rubisco activase deficiency on the temperature response of CO_2 assimilation rate and Rubisco activation state: Insights from transgenic tobacco with reduced amounts of Rubisco activase *Plant Physiol*. **151**, 2073-2082 (2009).

77 Sulpice, R. et al. Description and applications of a rapid and sensitive non-radioactive microplate-based assay for maximum and initial activity of D-ribulose-1,5-bisphosphate carboxylase/oxygenase. *Plant Cell Environ*. **30**, 1163-1175 (2007).

78 MacElroy Robert, D., Mack Henry, M. & Johnson Emmett, J. Properties of phosphoribulokinase from *Thiobacillus neapolitanus*. *J. Bacteriol*. **112**, 532-538 (1972).

79 Lee, J.-Y., Cheong, D.-E. & Kim, G.-J. A novel assay system for the measurement of

transketolase activity using xylulokinase from *Saccharomyces cerevisiae*. *Biotechnol. Lett*. **30**, 899-904 (2008).

80 Wang, X., Mann Craig, J., Bai, Y., Ni, L. & Weiner, H. Molecular cloning, characterization, and potential roles of cytosolic and mitochondrial aldehyde dehydrogenases in ethanol metabolism in *Saccharomyces cerevisiae*. *J. Bacteriol*. **180**, 822-830 (1998).

81 Livak, K. J. & Schmittgen, T. D. Analysis of relative gene expression data using real-time quantitative PCR and the $2^{-\Delta\Delta CT}$ method. *Methods* **25**, 402-408 (2001).

82 Burda, P. et al. Stepwise assembly of the lipid-linked oligosaccharide in the endoplasmic reticulum of *Saccharomyces cerevisiae*: Identification of the *ALG9* gene encoding a putative mannosyl transferase. *Proc. Natl. Acad. Sci. USA* **93**, 7160-7165 (1996).

83 Wang, Y., Parsons, L. R. & Su, X. AccuCor2: isotope natural abundance correction for dual-isotope tracer experiments. *Lab. Invest*. **101**, 1403-1410 (2021).

84 Cota-Sánchez, J. H., Remarchuk, K. & Ubayasena, K. Ready-to-use DNA extracted with a CTAB method adapted for herbarium specimens and mucilaginous plant tissue. *Plant Mol. Biol. Rep*. **24**, 161-167 (2006).

85 Sedlazeck, F. J. et al. Accurate detection of complex structural variations using single-molecule sequencing. *Nat. Methods* **15**, 461-468 (2018).

86 Cingolani, P. et al. A program for annotating and predicting the effects of single nucleotide polymorphisms, SnpEff. *Fly* **6**, 80-92 (2012).

87 Pertea, M. et al. StringTie enables improved reconstruction of a transcriptome from RNA-seq reads. *Nat. Biotechnol*. **33**, 290-295 (2015).

88 Shen, S. et al. rMATS: Robust and flexible detection of differential alternative splicing from replicate RNA-seq data. *Proc. Natl. Acad. Sci. USA* **111**, E5593-E5601 (2014).

89 Castell, C. H. & Smith, B. Measurement of formaldehyde in fish muscle using TCA extraction and the Nash reagent. *J. Fisheries Res.Board Can*. **30**, 91-98 (1973).

90 Kamiloglu, S., Sari, G., Ozdal, T. & Capanoglu, E. Guidelines for cell viability assays. *Food Frontiers* **1**, 332-349 (2020).

91 Sun, P., Zhang, H., Sun, Y. & Liu, J. The recent development of fluorescent probes for the detection of NADH and NADPH in living cells and *in vivo*. *Spectrochim. Acta A*. **245**, 118919 (2021).

92 Kong, A. T., Leprevost, F. V., Avtonomov, D. M., Mellacheruvu, D. & Nesvizhskii, A. I. MSFragger: ultrafast and comprehensive peptide identification in mass spectrometry–based proteomics. *Nat. Methods* **14**, 513-520 (2017).

93 Yu, F. et al. Fast quantitative analysis of timsTOF PASEF data with MSFragger and IonQuant. *Mol. Cell. Proteomics* **19**, 1575-1585 (2020).

Acknowledgments

This work was supported by the National Science Foundation of China (32401209), National Key R&D Program of China (2022YFA0912000), the Center of Synthetic Biology and Integrated Bioengineering (WU2022A006, WU2022A007, WU2023A009), Research Plan for Westlake University Funded Scientific Research Project (WU2022C032), Zhejiang Key Laboratory of Low-Carbon Intelligent Synthetic Biology (2024ZY01025), and Shenzhen Science and Technology Program (RCYX20231211090115013). We thank Wenwen Zhang and Xiaoyan Xu at Mass Spectrometry & Metabolomics Core Facility of Westlake University for MS analysis.

Author contributions

W.Z. and Y.W. conceived and designed the study. Y.W. supervised the project. W.Z. and N.L. performed the experiments and data processing, and analyzed the data. B.C. completed the analysis of the structure of Aox_m and $Adh2_m$, respectively. H.S. and X.F. were involved in constructing some of the engineered yeast strains needed for the study. W.Z. and Y.W. wrote and revised the manuscript with input of all authors. J.L., J.G., and B.W. contributed to the review, editing, and final approval of the manuscript. They provided valuable insights and suggestions to improve the quality of the research paper.

Competing interests

Authors declare no competing interests.

Figure legends

Fig. 1. Construction of MFF pathway and adaptive laboratory evolution. a. Schematic of the MFF pathway in CENPK2-1C. Gibbs free energy changes (ΔG) were calculated using eQuilibrator[43,44] (http://equilibrator.weizmann.ac.il) under the following conditions: pH 7.5, ionic strength 0.25 M, reactant concentrations 1 mM, and pMg 3.0. **b**. Activities of purified enzymes. The strains were precultured in the MM with glucose, washed twice using PBS (pH = 7.2), and then cultivated in MM with 20 g/L glucose at 30 °C, shaking at 180 rpm. **c**. ALE of SC-AOX$_0$. Stage I aimed to select mutants capable of growing in MM with 10 g/L MeOH. Stage II aimed to select strains with high tolerance and rapid growth in 20 g/L methanol. **d**. Growth profiles of SC-AOX$_9$ and SC-AOX$_{25}$ in MM with 10 g/L methanol. Sub-cultured SC-AOX$_{25}$ at time points I-VI during exponential growth exhibited different growth profile. All data represent the mean ± s.d. (n = 3 biologically independent samples). Metabolite abbreviations: *NAD*$^+$ nicotinamide adenine dinucleotide, *NADH* reduced nicotinamide adenine dinucleotide, *MFF* methanol-formate-formaldehyde. Enzyme abbreviations: methanol dehydrogenase (Mdh3), activator protein (Act1), alcohol oxidase (Aox), pyruvate carboxylase (Pyc1), catalase (Cat), formaldehyde dehydrogenase (Fld1), *S*-formylglutathione hydrolase (Fgh1), formate dehydrogenase (Fdh1). All abbreviations used in this article are listed in Supplementary Data 5. Source data are provided as a Source Data file.

Fig. 2. ^{13}C-isotopic analysis of the metabolites in SC-AOX$_{25}$ during methanol fermentation. a. ^{13}C-MeOH labeled amino acids. **b**. ^{13}C-MeOH labeled central metabolites. **c**. ^{13}C-formate labeled amino acids. **d**. ^{13}C-formate labeled central metabolites. **e**. $NaH^{13}CO_3$ labeled amino acids. **f**. $NaH^{13}CO_3$ labeled central metabolites. For ^{13}C labeling experiments, SC-AOX$_{25}$ was precultured three generations in MM with 10 g/L ^{13}C-MeOH (a and b), 10 g/L ^{12}C-MeOH with 0.5 g/L ^{13}C-formate (c and d), 10 g/L ^{12}C-MeOH with 0.5 g/L $NaH^{13}CO_3$ (e and f) before being sub-cultivated in the same medium but excluding serine and glycine, 30 °C, 180 rpm until middle log phase for analysis. All data represent the mean ± s.d. (n = 3 biologically independent samples). Metabolite

abbreviations: *MeOH* methanol, *Met* methionine, *Pro* proline, *Thr* threonine, *Ala* alanine, *Gly* glycine, *Asp* aspartic acid, *Ser* serine, *Tyr* tyrosine, *Glu* glutamicacid, *Asn* asparagine, *Phe* phenylalanine, *Lys* lysine, *Arg* arginine, *Orn* ornithine, *Cit* citrulline, *Val* valine, *Ile* isoleucine, *Pyr* pyruvate, *a-KG* alpha-ketoglutaric acid, *ATP* adenosine triphosphate, *F6P* fructose 6-phosphate, *R5P* ribose 5-phosphate, *FAD* flavin adenine dinucleotide, *2-PG* 2-phosphoglycerate, *3-PG* 3-phospho-D-glycerate, *F-1,6-BP* fructose 1,6-bisphosphate, *PEP* phosphoenolpyruvic acid, *G6P* glucose-6-phosphatase. Source data are provided as a Source Data file.

Fig. 3. Endogenous methanol assimilation pathways in SC-AOX$_{25}$. Purple arrows represent the reductive glycine pathway; blue arrows represent the glyoxylate-serine cycle; dark red arrows represent the pentose phosphate pathways; question marks represent uncoded pathways; the percentage shown for metabolites indicates the proportion of ^{13}C-labeled species relative to the total metabolite pool; The number beside the gene indicates the fold of increased transcript abundance. Metabolite abbreviations: *MeOH* methanol, fructose 6-phosphate, *R5P* ribose 5-phosphate, *2-PG* 2-phosphoglycerate, *3-PG* 3-phospho-D-glycerate, *F-1,6-BP* fructose 1,6-bisphosphate, *PEP* phosphoenolpyruvic acid, *G6P* glucose-6-phosphatase, *OAA* oxaloacetate, *GAP* glyceraldehyde 3-Phosphate, *DHAP* dihydroxyacetone phosphate, *S7P* sedoheptulose 7-phosphate, *E4P* erythrose 4-phosphate, *Xu5P* xylulose 5-phosphate, *Ru5P* ribulose 5-phosphate, *DHA* dihydroxyacetone. Enzyme abbreviations: alcohol dehydrogenase mutant (Adh2$_m$), transketolase (Tkl1, Tkl2), alcohol oxidase mutant (Aox$_m$), pyruvate carboxylase (Pyc1), dihydroxyacetone kinase (Dak1, Dak2), fructose-1,6-bisphosphatase (Fbp1), fructose 1,6-bisphosphate aldolase (Fba1), formate dehydrogenase (Fdh1), triose phosphate isomerase (Tpi1), phosphofructokinase (Pfk1, Pfk2), phosphoglucose isomerase (Pgi1), 6-phosphogluconatedehydrogenase (Gnd2), ribulose 5-phosphate epimerase (Rpe1), ribose-5-phosphate ketol-isomerase (Rki1), transaldolase (Nqm1, Tal1), mitochondrial pyruvate carrier (Mpc3), pyruvate dehydrogenase alpha (Pda1), alanine:glyoxylate aminotrans(X)ferase (Agx1), cytosolic serine hydroxymethyltransferase (Shm2), catabolic L-serine (L-threonine) deaminase

(Cha1), cytoplasmic malate dehydrogenase (Mdh2), pyruvate kinase (Pyk1, Pyk2), phosphopyruvate hydratase (Eno1, Eno2), putative phosphopyruvate hydratase (Err1, Err2, Err3), ATP-binding protein (Tda10), glyoxylate reductase (Gor1), Formate-tetrahydrofolate ligase (Ade3), methenyltetrahydrofolate cyclohydrolase (Ade3), methylenetetrahydrofolate dehydrogenase (Ade3), mitochondrial C1-tetrahydrofolate synthase (Mis1), mitochondrial serine hydroxymethyltransferase (Shm1), mitochondrial glycine decarboxylase complex (Gcv1, Gcv2, Gcv3).

Fig. 4. **Elucidation of energy modules and their correlations with ATP/NADH production, methanol growth, and consumption in engineered methylotrophic *S. cerevisiae*.** **a** and **b**. Comparison of ATP (**a**) and NADH (**b**) levels in SC-AOX$_{25}$, SC-AOX$_0$, and CEN.PK2-1C. **c**. Cell density of different mutants in MM with methanol, glucose, or methanol plus glucose. (strains represent SC-AOX$_0$, CEN.PK2-1C, SC-AOX$_{25}$-Δ$FDH1_{hp}$, SC-AOX$_{25}$-Δ$FDH1sc$-Δ$FDH1_{hp}$, SC-AOX$_0$-AOX_m, or SC-AOX$_0$-$ADH2_m$). **d**. Methanol consumption of different mutants in MM with methanol, glucose, or methanol-coupled glucose. **e** and **f**. ATP (**e**) and NADH (**f**) levels in different mutants in MM with methanol, glucose, and methanol plus glucose. The strains were precultured in MM with 10 g/L MeOH, MM with 20 g/L glucose plus 10 g/L methanol (†), or MM with 20 g/L glucose (‡) to the middle log phase, washed twice with PBS at pH 7.2, and then sub-cultured in the same medium. All data represent the mean ± s.d. (n = 3 biologically independent samples). Statistical analysis was performed using a two-tailed Student's *t*-test ($^{*}P < 0.05$, $^{**}P < 0.01$, $^{***}P < 0.001$, $^{****}P < 0.0001$, "ns" stands for "not significant"). Source data are provided as a Source Data file.

Fig. 5. Engineering CBB cycle in SC-AOX$_{25}$. **a**. Heterologous CBB pathway. **b**. Enzymatic activities of Rubisco and Prk. **c**. Growth profiles of the SC-AOX$_{25}$-CBB in MM with 10 g/L methanol. **d**. NaH^{13}CO$_3$ labeled central metabolites in SC-AOX$_{25}$-CBB. **e**. ^{13}C-MeOH labeled central metabolites in SC-AOX$_{25}$-CBB. **f**. ^{13}C-formate labeled central metabolites in SC-AOX$_{25}$-

CBB. For ^{13}C labeling experiments, SC-AOX$_{25}$ was precultured three generations in MM with 10 g/L ^{12}C-MeOH with 0.5 g/L NaH^{13}CO$_3$ (d), 10 g/L ^{13}C-MeOH with 0.5 g/L NaH^{12}CO$_3$ (e), 10 g/L ^{12}C-MeOH with 0.5 g/L ^{13}C-formate (f) before being sub-cultivated in the same medium but excluding serine and glycine, 30 °C, 180 rpm until middle log phase for analysis. All data represent the mean ± s.d. (n = 3 biologically independent samples). Metabolite abbreviations: *RuBP* ribulose-1,5-disphosphate, *ADP* adenosine diphosphate, *ATP* adenosine triphosphate, *NAD*$^+$ nicotinamide adenine dinucleotide, *NADH* reduced nicotinamide adenine dinucleotide, *MFF* methanol-formate-formaldehyde, *PPP* pentose phosphate pathway, *F6P* fructose 6-phosphate, *3-PGP* 3-phospho-D-glyceroyl-phosphate, *3-PG* 3-phospho-D-glycerate, *GAP* glyceraldehyde 3-Phosphate, *F-1,6-BP* fructose 1,6-bisphosphate, *Ru5P* ribulose 5-phosphate, *a-KG* alpha-ketoglutaric acid, *R5P* ribose 5-phosphate, *2-PG* 2-phosphoglycerate. Enzyme abbreviations: phosphoribulokinase (Prk), fructose-1,6-bisphosphatase (Fbp1), glyceraldehyde-3-phosphate dehydrogenase (Tdh1, Tdh2, Tdh3), 3-phosphoglycerate kinase (Pgk1), chaperone proteins of Rubisco (groEl, groES), ribulose -1,5-bisphosphate carboxylase/oxygenase (Rubisco). Source data are provided as a Source Data file.

Fig. 6. DPC in SC-AOX$_{25}$ and proteomics characterization. a. TEM images of DPC products from different growth stages of SC-AOX$_{25}$ at different methanol concentration and their uncrosslinked forms. The experiment was conducted with two biological replicates under identical OD$_{600}$ conditions. Similar DPC cross-linking patterns were observed in both replicate results. **b**. Venn diagram of the DPC associated proteins. **c**. Quantitative proteomics analysis of the proteins from crosslinked DPC of SC-AOX$_{25}$ at various methanol concentrations. Strains in the late exponential growth phase were selected for proteomics analysis. 29 out of 66 common top hits ranked by average abundance are presented. Enzyme abbreviations: heat shock protein (Hsp82), pyruvate DeCarboxylase (Pdc1), Hsp70 family ATP-binding protein (Ssa1, Ssa2), phosphopyruvate hydratase (Eno2), glyceraldehyde-3-phosphate dehydrogenase isozyme (Tdh3), formate dehydrogenase (Fdh1), highly variable glycoprotein localized to cell wall via GPI anchor

(Css1), 3-phosphoglycerate kinase (Pgk1), mitochondrial aldehyde dehydrogenase (Ald4), cytoplasmic ATPase (Ssb2), RNA binding protein involved in synthesis of 18S and 5.8S rRNAs (Rrp5), putative substrate of cAMP-dependent protein kinase (Cub1), pyruvate kinase (Cdc19), GPI-anchored protein (Ecm33), acetohydroxyacid reductoisomerase and mtDNA binding protein (Ilv5), ATPase component of heat shock protein Hsp90 chaperone complex (Sse1), Translational elongation factor (Tef1), tetradecameric mitochondrial chaperonin (Hsp60), elongation factor (Eft1), inositol-3-phosphate synthase (Ino1), Acetyl-CoA carboxylase (Fas3), tetrameric phosphoglycerate mutase (Gpm1), alcohol dehydrogenase (Adh2), fructose 1,6-bisphosphate aldolase (Fba1), alpha subunit of fatty acid synthetase (Fas2), ATPase involved in protein import into the ER (Kar2), Hsp70 family ATPase (Ssc1), subunit 2 of ubiquinol cytochrome-c reductase (Qcr2). Source data are provided as a Source Data file.

Editor's Summary

Synthetic methylotrophic *S. cerevisiae* often faces energetic constrains during one-carbon assimilation. Here, the authors address this issue by engineering of heterologous methanol-formate-formaldehyde oxidation pathways to enable CO2 assimilation *via* non-native Calvin cycle during methanol fermentation.

Peer review information: *Nature Communications* thanks Wenming Zhang and the other, anonymous, reviewer(s) for their contribution to the peer review of this work. A peer review file is available.

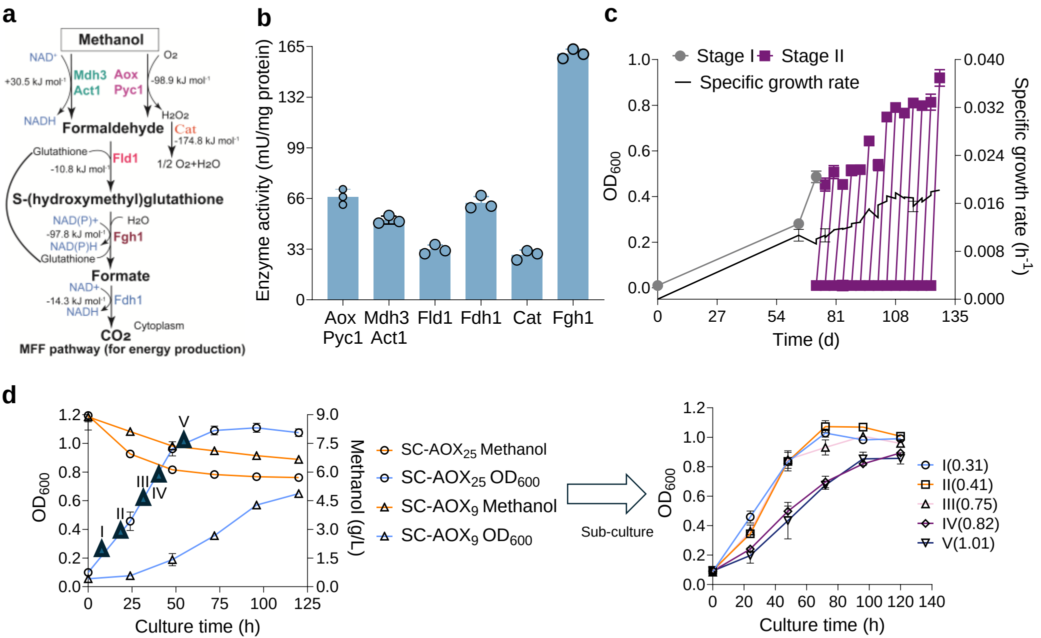
a
Methanol
NAD+
Mdh3 Aox
Act1 Pyc1
O2
+30.5 kJ mol-1
-98.9 kJ mol-1
NADH
H2O2
Formaldehyde
Cat
-174.8 kJ mol-1
1/2 O2+H2O
Glutathione
Fld1
-10.8 kJ mol-1
S-(hydroxymethyl)glutathione
NAD(P)+
H2O
-97.8 kJ mol-1
Fgh1
NAD(P)H
Glutathione
Formate
NAD+
-14.3 kJ mol-1
Fdh1
NADH
Cytoplasm
CO2
MFF pathway (for energy production)
b
Enzyme activity (mU/mg protein)
165
132
99
66
33
0
Aox Pyc1
Mdh3 Act1
Fld1
Fdh1
Cat
Fgh1
c
Stage I
Stage II
Specific growth rate
OD600
1.0
0.8
0.6
0.4
0.2
0.0
0.040
0.032
0.024
0.016
0.008
0.000
Specific growth rate (h-1)
0
27
54
81
108
135
Time (d)
d
OD600
1.2
1.0
0.8
0.6
0.4
0.2
0.0
9.0
7.5
6.0
4.5
3.0
1.5
0.0
Methanol (g/L)
I
II
III
IV
V
0
25
50
75
100
125
Culture time (h)
SC-AOX25 Methanol
SC-AOX25 OD600
SC-AOX9 Methanol
SC-AOX9 OD600
Sub-culture
OD600
1.2
1.0
0.8
0.6
0.4
0.2
0.0
0
20
40
60
80
100
120
140
Culture time (h)
I(0.31)
II(0.41)
III(0.75)
IV(0.82)
V(1.01)

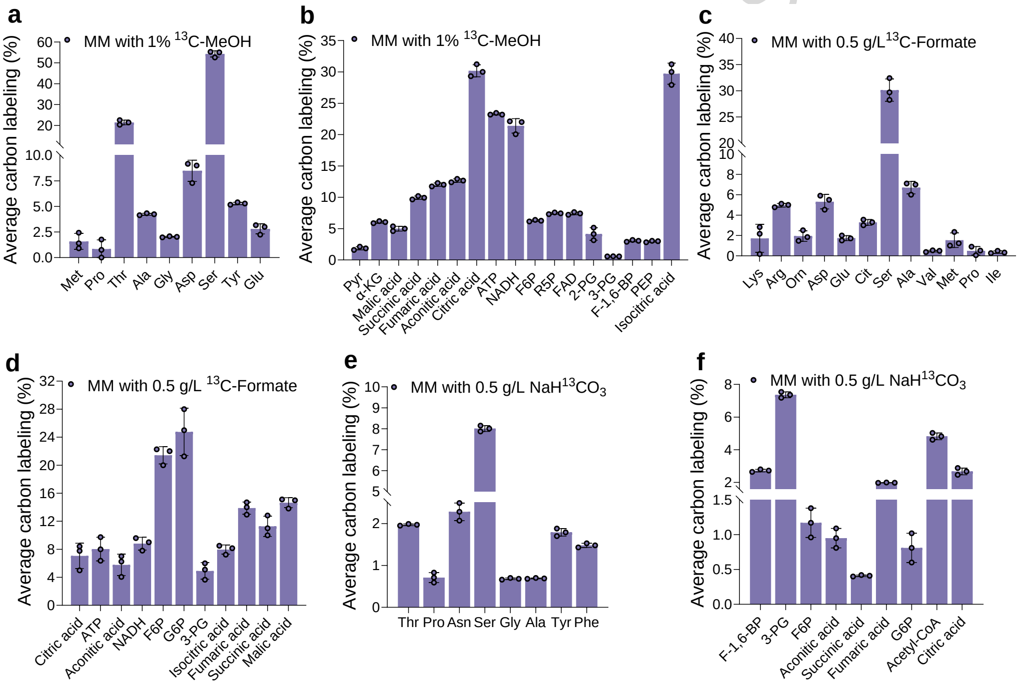
a
MM with 1% ^{13}C-MeOH
Average carbon labeling (%)
60
50
40
30
20
10.0
7.5
5.0
2.5
0.0
Met
Pro
Thr
Ala
Gly
Asp
Ser
Tyr
Glu
b
MM with 1% ^{13}C-MeOH
Average carbon labeling (%)
35
30
25
20
15
10
5
0
Pyr
α-KG
Malic acid
Succinic acid
Fumaric acid
Aconitic acid
Citric acid
ATP
NADH
F6P
R5P
FAD
2-PG
3-PG
F-1,6-BP
PEP
Isocitric acid
c
MM with 0.5 g/L ^{13}C-Formate
Average carbon labeling (%)
40
35
30
25
20
10
8
6
4
2
0
Lys
Arg
Orn
Asp
Glu
Cit
Ser
Ala
Val
Met
Pro
Ile
d
MM with 0.5 g/L ^{13}C-Formate
Average carbon labeling (%)
32
28
24
20
16
12
8
4
0
Citric acid
ATP
Aconitic acid
NADH
F6P
G6P
3-PG
Isocitric acid
Fumaric acid
Succinic acid
Malic acid
e
MM with 0.5 g/L NaH^{13}CO$_3$
Average carbon labeling (%)
10
9
8
7
6
5
2
1
0
Thr
Pro
Asn
Ser
Gly
Ala
Tyr
Phe
f
MM with 0.5 g/L NaH^{13}CO$_3$
Average carbon labeling (%)
8
6
4
2
1.5
1.0
0.5
0.0
F-1,6-BP
3-PG
F6P
Aconitic acid
Succinic acid
Fumaric acid
G6P
Acetyl-CoA
Citric acid

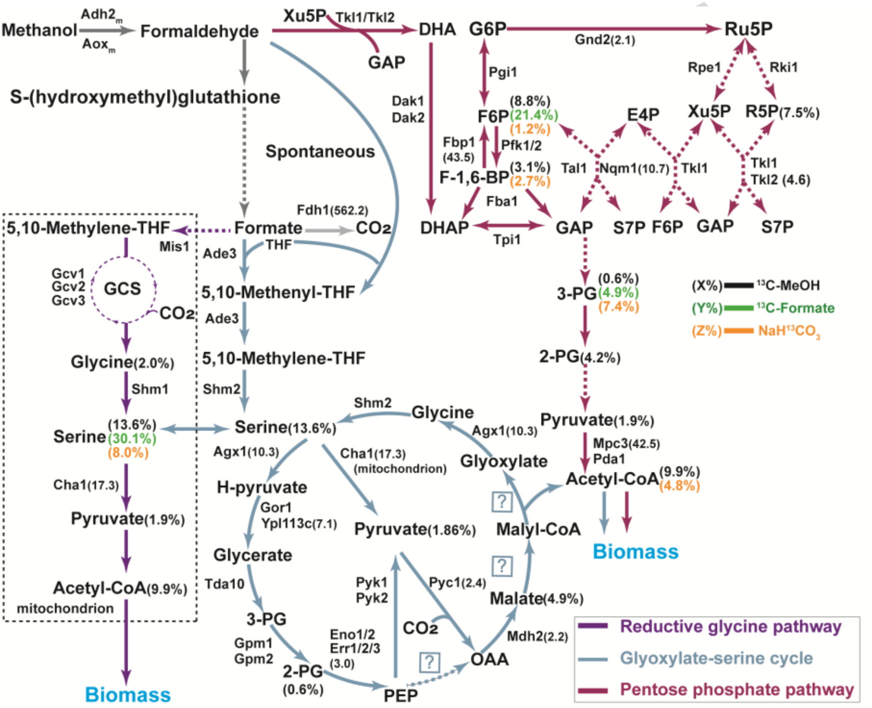

The percentage beside the metabolites indicates the proportion of ^{13}C-labeled species for metabolite.

The number beside the gene indicates the transcript abundance of genes.

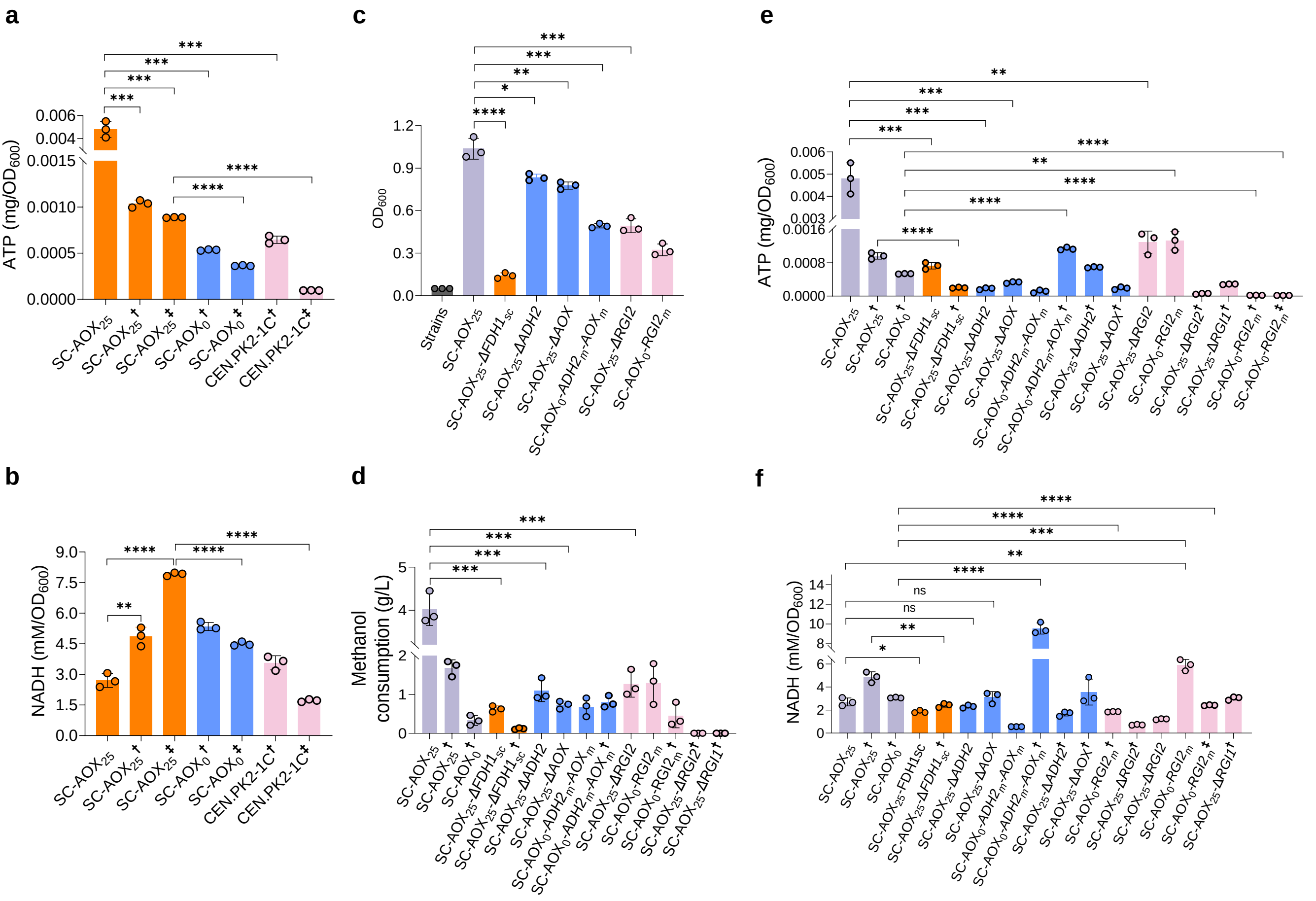
a
ATP (mg/OD600)
0.0000
0.0005
0.0010
0.0015
0.004
0.006
***
***
***
***
****
****
SC-AOX25
SC-AOX25†
SC-AOX25‡
SC-AOX0†
SC-AOX0‡
CEN.PK2-1C†
CEN.PK2-1C‡
b
NADH (mM/OD600)
0.0
1.5
3.0
4.5
6.0
7.5
9.0
**
****
****
****
SC-AOX25
SC-AOX25†
SC-AOX25‡
SC-AOX0†
SC-AOX0‡
CEN.PK2-1C†
CEN.PK2-1C‡
c
OD600
0.0
0.3
0.6
0.9
1.2
***
***
**
*
****
Strains
SC-AOX25
SC-AOX25-ΔFDH1sc
SC-AOX25-ΔADH2
SC-AOX25-ΔAOX
SC-AOX0-ADH2m-AOXm
SC-AOX25-ΔRGI2
SC-AOX0-RGI2m
d
Methanol consumption (g/L)
0
1
2
4
5
***
***
***
***
SC-AOX25
SC-AOX25†
SC-AOX0†
SC-AOX25-ΔFDH1sc
SC-AOX25-ΔFDH1sc†
SC-AOX25-ΔADH2
SC-AOX25-ΔAOX
SC-AOX0-ADH2m-AOXm
SC-AOX0-ADH2m-AOXm†
SC-AOX25-ΔRGI2
SC-AOX0-RGI2m
SC-AOX0-RGI2m†
SC-AOX25-ΔRGI2†
SC-AOX25-ΔRGI1†
e
ATP (mg/OD600)
0.0000
0.0008
0.0016
0.003
0.004
0.005
0.006
**
***
***
***
****
**
****
****
****
SC-AOX25
SC-AOX25†
SC-AOX0†
SC-AOX25-ΔFDH1sc
SC-AOX25-ΔFDH1sc†
SC-AOX25-ΔADH2
SC-AOX25-ΔAOX
SC-AOX0-ADH2m-AOXm
SC-AOX0-ADH2m-AOXm†
SC-AOX25-ΔADH2†
SC-AOX25-ΔAOX†
SC-AOX25-ΔRGI2
SC-AOX0-RGI2m
SC-AOX25-ΔRGI2†
SC-AOX25-ΔRGI1†
SC-AOX0-RGI2m†
SC-AOX0-RGI2m‡
f
NADH (mM/OD600)
0
2
4
6
8
10
12
14
****
****
***
**
****
ns
ns
**
*
SC-AOX25
SC-AOX25†
SC-AOX0†
SC-AOX25-FDH1sc
SC-AOX25-ΔFDH1sc†
SC-AOX25-ΔADH2
SC-AOX25-ΔAOX
SC-AOX0-ADH2m-AOXm
SC-AOX0-ADH2m-AOXm†
SC-AOX25-ΔADH2†
SC-AOX25-ΔAOX†
SC-AOX0-RGI2m†
SC-AOX25-ΔRGI2†
SC-AOX25-ΔRGI2
SC-AOX0-RGI2m
SC-AOX0-RGI2m‡
SC-AOX25-ΔRGI1†

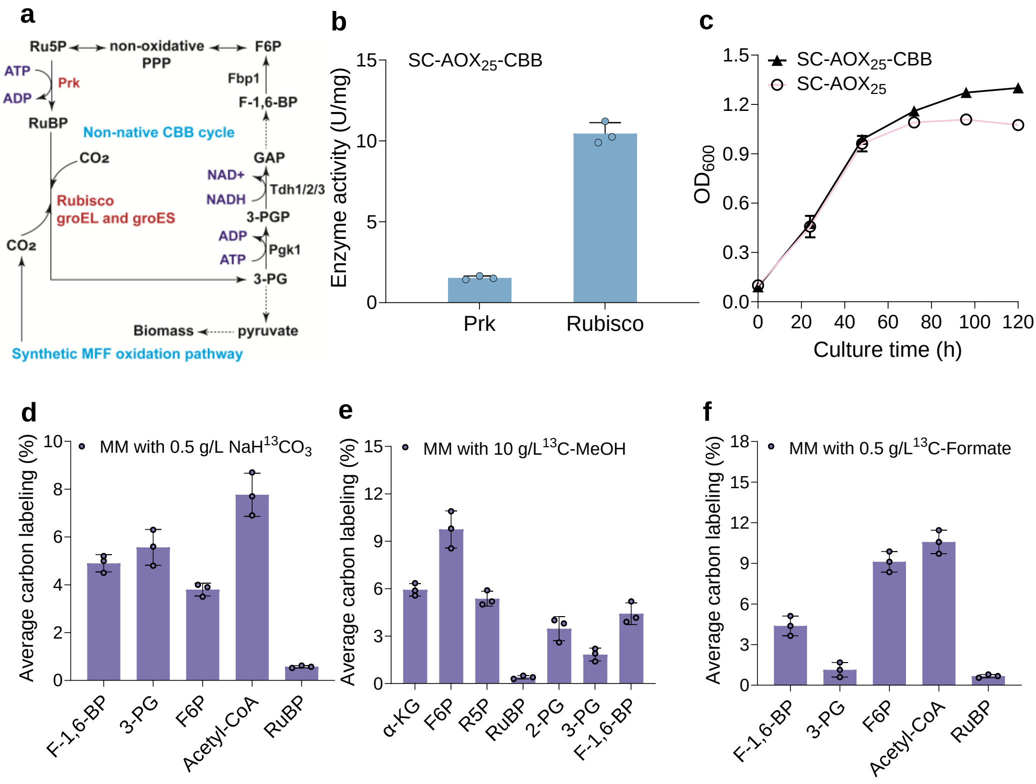
a
Ru5P
non-oxidative PPP
F6P
ATP
ADP
Prk
Fbp1
F-1,6-BP
RuBP
Non-native CBB cycle
CO₂
GAP
NAD+
NADH
Tdh1/2/3
Rubisco
groEL and groES
3-PGP
ADP
ATP
Pgk1
CO₂
3-PG
Biomass
pyruvate
Synthetic MFF oxidation pathway
b
SC-AOX$_{25}$-CBB
Enzyme activity (U/mg)
0
5
10
15
Prk
Rubisco
c
SC-AOX$_{25}$-CBB
SC-AOX$_{25}$
OD$_{600}$
0.0
0.3
0.6
0.9
1.2
1.5
0
20
40
60
80
100
120
Culture time (h)
d
MM with 0.5 g/L NaH^{13}CO$_3$
Average carbon labeling (%)
0
2
4
6
8
10
F-1,6-BP
3-PG
F6P
Acetyl-CoA
RuBP
e
MM with 10 g/L ^{13}C-MeOH
Average carbon labeling (%)
0
3
6
9
12
15
α-KG
F6P
R5P
RuBP
2-PG
3-PG
F-1,6-BP
f
MM with 0.5 g/L ^{13}C-Formate
Average carbon labeling (%)
0
3
6
9
12
15
18
F-1,6-BP
3-PG
F6P
Acetyl-CoA
RuBP

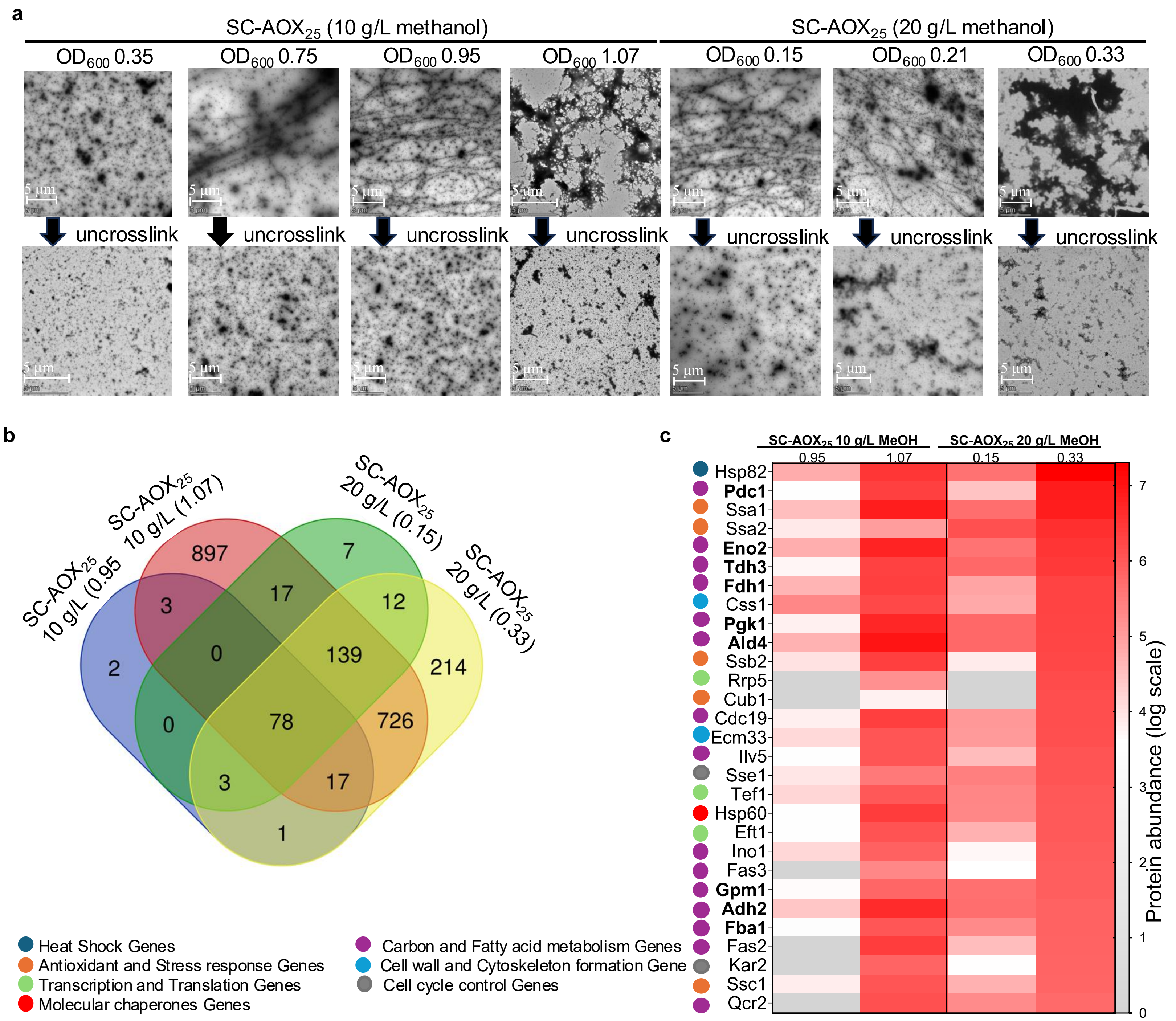
a
SC-AOX$_{25}$ (10 g/L methanol)
SC-AOX$_{25}$ (20 g/L methanol)
OD$_{600}$ 0.35
OD$_{600}$ 0.75
OD$_{600}$ 0.95
OD$_{600}$ 1.07
OD$_{600}$ 0.15
OD$_{600}$ 0.21
OD$_{600}$ 0.33
uncrosslink
5 µm
b
SC-AOX$_{25}$ 10 g/L (0.95
SC-AOX$_{25}$ 10 g/L (1.07)
SC-AOX$_{25}$ 20 g/L (0.15)
SC-AOX$_{25}$ 20 g/L (0.33)
897
7
3
17
12
2
0
139
214
0
78
726
3
17
1
● Heat Shock Genes
● Antioxidant and Stress response Genes
● Transcription and Translation Genes
● Molecular chaperones Genes
● Carbon and Fatty acid metabolism Genes
● Cell wall and Cytoskeleton formation Gene
● Cell cycle control Genes
c
SC-AOX$_{25}$ 10 g/L MeOH
SC-AOX$_{25}$ 20 g/L MeOH
0.95
1.07
0.15
0.33
Hsp82
Pdc1
Ssa1
Ssa2
Eno2
Tdh3
Fdh1
Css1
Pgk1
Ald4
Ssb2
Rrp5
Cub1
Cdc19
Ecm33
Ilv5
Sse1
Tef1
Hsp60
Eft1
Ino1
Fas3
Gpm1
Adh2
Fba1
Fas2
Kar2
Ssc1
Qcr2
Protein abundance (log scale)
0
1
2
3
4
5
6
7